The Plasma Structure of Coronal-Hole Solar Wind: Origins and Evolution

Joseph E. Borovsky[1,2]

1 Space Science Institute, Boulder, Colorado

2 University of Michigan, Ann Arbor, Michigan

Whereas slow solar wind is known to be highly structured, the fast (coronal-hole-origin) wind is usually considered to be homogeneous. Using measurements from Helios 1+2, ACE, Wind, and Ulysses, structure in the coronal-hole-origin solar wind is examined from 0.3 AU to 2.3 AU. Care is taken to collect and analyze intervals of "unperturbed coronal-hole plasma". In these intervals, solar-wind structure is seen in the proton number density, proton temperature, proton specific entropy, magnetic-field strength, magnetic field to density ratio, electron heat flux, helium abundance, heavy-ion charge-state ratios, and Alfvenicity. Typical structure amplitudes are factors of two, far from homogeneous. Variations are also seen in the solar wind radial velocity. Using estimates of the motion of the solar-wind-origin footpoint on the Sun for the various spacecraft, the satellite time-series measurements are converted to distance along the photosphere. Typical variation scale lengths for the solar-wind structure are several variations per supergranule. The structure amplitude and structure scale sizes do not evolve with distance from the Sun from 0.3 to 2.3 AU. An argument is quantified that these variations are the scale expected for solar-wind production in open magnetic-flux funnels in coronal holes. Additionally, a population of magnetic-field foldings (switchbacks, reversals) in the coronal-hole plasma is examined: this population evolves with distance from the Sun such that the magnetic-field is mostly Parker-spiral aligned at 0.3 AU and becomes more misaligned with distance outward.

1. Introduction

There is generally considered to be three types of solar-wind plasma: fast wind, slow wind, and ejecta [cf. *Richardson et al.*, 2000; *Neugebauer et al.*, 2003; *Zhao et al.*, 2009; *Reisenfeld et al.*, 2013]. A recent categorization by *Xu and Borovsky* [2015] (see also

Antonucci et al. [2005], *Schwenn* [2006], and *Susino et al.* [2008]) separates the solar-wind plasma into four types: coronal-hole-origin plasma (fast wind), streamer-belt-origin plasma, sector-reversal-region plasma, and ejecta. The open magnetic flux of active regions on the Sun can also be a source of (mainly slow) solar wind [e.g. *Kojima et al.,* 1999; *van Driel-Gesztelyi et al.*, 2012; *Slemzin et al.*, 2013; *Culhane et al.*, 2014]

Coronal-hole-origin plasma (fast wind) is known to originate from the open-flux coronal-hole regions on the Sun [*Krieger et al.*, 1973; *Bame et al.*, 1976; *Levine et al.*, 1977]. Coronal-hole-origin solar wind is noted for low number densities [*Belcher and Davis,* 1971], high proton entropies [*Burlaga et al.*, 1990; *Borovsky and Denton,* 2010], and low heavy-ion charge-state ratios [*Zurbuchen et al.*, 2002; *von Steiger et al.*, 2010]. Coronal-hole-origin solar wind is characterized by the presence of He^{++} beams moving ahead of the protons by a large fraction of a proton Alfven speed [e.g. *Marsch et al.*, 1982; *Neugebauer et al.*, 1996] and coronal-hole-origin solar wind is characterized by a well-defined unidirectional electron strahl [*Feldman et al.*, 1978; *Fitzenreiter et al.*, 1998; *Hammond et al.*, 1996]. The protons and alpha particles of the coronal-hole-origin solar wind exhibit heating (increasing specific entropy) with distance from the Sun in the inner heliosphere [*Schwenn et al.*, 1981; *Freeman and Lopez*, 1985; *Hellinger et al.*, 2011; *Borovsky and Gary*, 2014].

Coronal-hole-origin solar-wind plasma is filled with current sheets (directional discontinuities) [*Siscoe et al.,* 1968; *Vasquez et al.*, 2007], as are the other types of solar-wind plasma, the current sheets of the coronal-hole-origin plasma and streamer-belt-origin plasma are Alfvenic [*Neugebauer*, 1985], with the coronal-hole-origin current sheets being the most Alfvenic [*Borovsky and Denton*, 2010]. The current sheets being Alfvenic means they are co-located with velocity shears [*De Keyser et al.*, 1998; *Neugebauer*, 2006]. Across the current sheets of the coronal-hole-origin plasma the solar-wind magnetic field can rotate by 90° or more and the vector velocity of the solar wind can jump by the Alfven speed [*Borovsky*, 2012a]. The abrupt velocity vector jump can have a magnetosonic Mach number $M_{ms} \sim 0.8$ [*Borovsky and Steinberg*, 2014].

Coronal-hole-origin plasma is sometimes considered to be structure free or relatively homogeneous compared with slower solar wind [e.g. *Bame et al.*, 1977; *Parhi et al.*, 1999; *Bavassano et al.*, 2004; *Borovsky*, 2012b; *Poletto*, 2013; *Podesta,* 2013], however it is not

homogeneous. As will be seen in this study, the unperturbed intervals of coronal-hole-origin plasma show factor-of-2 variations in the number density, temperature, magnetic-field strength, helium abundance, heavy-ion charge-state ratios, electron-strahl intensity, and proton specific entropy. Well-known examples of plasma structure in the coronal-hole-origin solar wind are the microstreams of the polar solar wind [*Neugebauer et al.*, 1995, 1997; *Neugebauer*, 2012] and pressure-balance structures at low and high latitudes [*Thieme et al.*, 1990; *Reisenfeld et al.*, 1999]. Connections have been explored between microstreams in the coronal-hole-origin solar wind and polar plumes [*Neugebauer et al.*, 1997] and x-ray jets [*Neugebauer*, 2012] seen at the Sun and connections have been explored between pressure-balance structures in the solar wind and supergranules [*Thieme et al.*, 1989] and macrospicules and polar plumes [*Thieme et al.*, 1990; *McComas et al.,* 1995; *Reisenfeld et al.*, 1999; *Yamauchi et al.*, 2002, 2003].

In this report structure in the coronal-hole-origin solar wind will be examined from 0.3 to 2.3 AU using the Helios 1+2, ACE, Wind, and Ulysses spacecraft. Care will be taken to collect and analyze intervals of "unperturbed coronal-hole plasma" that are not compressed or rarefied. Structure as measured by the proton number density, proton temperature, proton specific entropy, magnetic-field strength, helium abundance, heavy-ion charge-state ratios, electron-strahl intensity, and Alfvenicity will be examined. Measurements of structure at different distances from the Sun on different spacecraft will be compared by converting the time series of measurements into distance along the photosphere.

This manuscript is outlined as follows. In Section 2 the data sets utilized in the present study are described. In Section 3 the collected intervals of unperturbed coronal-hole plasma are described: intervals at 1 AU in the ecliptic plane in section 3.1, intervals at 0.3 and 0.6 AU in the ecliptic plane in Section 3.2, and intervals at ~2.3 AU over the poles in Section 3.3. Section 4 describes the nature of structure seen in the coronal-hole-origin solar wind and examines correlations between the various quantities measured in coronal-hole-origin solar wind. In Section 5.1 factors are developed to convert spacecraft time series into distance along the photosphere of the solar-wind-origin footpoint. In Section 5.2 those conversions are utilized to compare structure measured by different spacecraft at different distances from the Sun. The analysis of structure in the coronal-hole-origin solar wind is summarized in Section

6. Section 7.1 discusses the expected structure sizes in solar wind emanating from coronal holes and Section 7.2 estimates the effects of solar-wind turbulence on structure in the coronal-hole-origin plasma.

2. Data Sets Utilized

To study unperturbed coronal-hole plasma with the Helios 1+2 spacecraft near the Sun, with the Wind and ACE (Advanced Composition Explorer) spacecraft at 1 AU, and with the Ulysses spacecraft in polar crossings at ~2 AU, several data sets will be utilized.

At 1 AU plasma measurements with 64-s time resolution from ACE SWEPAM (Solar Wind Electron Proton Alpha Monitor) [*McComas et al.*, 1998] will be utilized along with merged magnetic-field measurements from ACE MAG (Magnetometer) [*Smith et al.*, 1998]. Heavy-ion measurements from ACE SWICS (Solar Wind Ion Composition Monitor) [*Gloeckler et al.*, 1998] (version 1p1) are also used for events prior to Day 233 of 2011. To check ACE SWEPAM measurements of the α/p density ratio, fitted measurements from the Faraday cups on Wind SWE (Solar Wind Experiment) [*Ogilvie et al.*, 1995; *Kasper et al.*, 2006] are used. For higher-time-resolution measurements of the solar wind at 1 AU the 3-s plasma measurements of Wind 3DP (3D Plasma Analyzer) [*Lin et al.,* 1995] and the 3-s magnetic-field measurements from Wind MFI (Magnetic Field Investigation) [*Lepping et al.*, 1995] are also utilized. Hourly averaged values of solar wind quantities from the multispacecraft OMNI2 data set [*King and Papitashvili*, 2005] will also be utilized.

In the inner heliosphere the 40-s time-resolution merged plasma and magnetic-field data set from Helios 1 and Helios 2 [*Rosenbauer et al.*, 1977; *Denskat and Neubauer*, 1982] is utilized.

From Ulysses, plasma measurements from SWOOPS (Solar Wind Observations Over the Poles of the Sun) [*Bame et al.*, 1992] with 4-min time resolution and magnetic-field measurements from VHM (Vector Helium Magntometer) [*Balogh et al.*, 1992] with 1-min time resolution are used.

3. Intervals of Unperturbed Coronal-Hole Plasma

For the study of structure in coronal-hole-origin solar-wind plasma, intervals of unperturbed coronal-hole plasma are collected and cataloged in Table 1 (at 1 AU), in Table 2 (at 0.3 and 0.6 AU), and in Table 3 (at ~2 AU).

3.1. Flattop High-Speed Streams at 1 AU

The first collection of unperturbed coronal-hole plasma is comprised of a selection of 66 27-day repeating high-speed streams at 1 AU that have each attained a maximum velocity and which each approximately maintain that velocity for a day or so. (See *Feldman et al.* [1976a] for an early collection of such events.) The temporal profile of the solar-wind velocity for the selected high-speed streams has a "flattop like" shape owing to the velocity plateau. These intervals are cataloged in Table 1. This selection of 66 events is much more restrictive than a general collection of high-speed streams [e.g. *Xystouris et al.*, 2014]. An example of such a flattop high-speed stream (Flattop12) is shown in Figure 1. The portion of the flattop velocity that is chosen to represent unperturbed coronal-hole plasma commences when the solar-wind magnetic-field strength drops to a more-or-less constant value early in the flattop region (cf. bottom panel of Figure 1). The region of elevated magnetic field that is eliminated is considered to be compressed coronal-hole plasma at the end of the corotating interaction region (CIR) prior in time to the unperturbed coronal-hole plasma. The termination of the flattop event is taken to be the point in time at which the solar-wind velocity begins to systematically drop (cf. top panel of Figure 1): this point is believed to be the onset of the rarefaction region on the trailing edge of the high-speed stream [cf. *Borovsky and Denton*, 2016]. Other plasma parameters are examined to ensure that the flattop region does not contain ejecta-like plasma: the event is eliminated if there is an extended (multi-hour) interval of non-ecliptic magnetic-field direction (indicating ejecta) [*Lepping et al.*, 2005; *Borovsky*, 2010], if there is a region of anomalously low proton temperature (signaling three-dimensional expansion, again ejecta) [*Gosling et al.*, 1973; *Elliott et al.,* 2005], or if there is a region of bidirectional strahl (again indicating the possibility of ejecta) [*Gosling et al.*, 1987; *Richardson and Cane*, 2010].

In the catalog of 66 intervals of unperturbed coronal-hole plasma (flattop intervals) at 1 AU in Table 1, the onset and termination times of the chosen intervals of the flattops are

listed, the times of the leading-edge stream interface prior to each flattop interval are listed, and the times of the trailing-edge stream interface following each flattop interval are listed. The leading edge stream interface is taken to be the point in time at which the proton specific entropy $S_p = T_p/n_p^{2/3}$ crosses from below $S_p = 4$ eV cm^2 to above $S_p = 4$ eV cm^2 [cf. *Borovsky and Denton*, 2010], usually in a sudden jump. This signifies the time at which the spacecraft crosses from low-entropy streamer-belt plasma into high entropy coronal-hole plasma [*Burlaga et al.*, 1990; *Siscoe and Intriligator*, 1993]. The trailing edge stream interface is more difficult to identify: *Borovsky and Denton* [2016] find the best indication of the trailing-edge stream interface to be an inflection point in the velocity-versus-time plot for the trailing edge of the high-speed stream. This inflection point is believed to be the center point (maximum rarefaction) of the trailing-edge rarefaction and hence a good choice for the boundary between fast coronal-hole plasma and slow streamer-belt plasma. In Table 2 the width (temporal duration) W_{flat} of the unperturbed coronal-hole plasma and the width (temporal duration) W_{hss} of the high-speed stream (time of leading-edge stream interface to the time of trailing-edge steam interface) are listed for each flattop interval. In the collection, the widths W_{flat} of the intervals of unperturbed coronal-hole solar wind vary from 22 hr to 123 hr.

In the top panel of Figure 2 the average solar-wind radial velocity $<v_r>$ in each of the 66 intervals of Table 1 is plotted as a function of the width W_{flat} of the flattop regions. The Pearson linear correlation coefficient between $<v_r>$ and W_{flat} is $R_{corr} = +0.13$. For 66 independent data points, significant correlation (2-sigma level) occurs for $|R_{corr}| > 0.24$, so $<v_r>$ and W_{flat} are uncorrelated. In the bottom panel of Figure 2 the average solar-wind velocity $<v_r>$ for each of the 66 flattop intervals is plotted as a function of the width W_{hss} of the high-speed streams: the Pearson linear correlation coefficient between $<v_r>$ and W_{hss} is $R_{corr} = +0.45$, a significant correlation with $|R_{corr}| > 0.24$ being the 2-sigma level of correlation. In the bottom panel a linear regression to the data is plotted as the blue dashed line. In both panels of Figure 2 high-speed streams identified by *Ko et al.* [2014] as originating in polar coronal holes are marked with a red central dot and high-speed streams identified by *Ko et al.* [2014] as originating in equatorward extensions of coronal holes are marked with a green central dot.

Table 4 lists the average of the 66 mean values of several quantities for the 66 flattop intervals of Table 1. In Table 5 the Pearson linear correlation coefficients R_{corr} between the 66 values of the various averaged quantities are listed. Significant correlation occurs for $|R_{corr}|$ > 0.24. Some of the stronger correlations to note in Table 5 are the following. There are strong positive correlations between the width W_{hss} of the coronal-hole stream and the averaged value of the solar-wind radial velocity $<v_r>$, the averaged value of the magnetic-field strength $<B_{mag}>$, and the averaged value of the radial component of the magnetic field $|<B_r>|$ (where the absolute value of the individual averages $<B_r>$ are taken since some coronal holes are in toward sectors and some are in away sectors). A related set of correlations are the strong positive correlations between $<v_r>$, $<B_{mag}>$, and $|<B_r>|$, probably caused by the open-flux expansion factor being inversely related to W_{hss} [*Levine et al.*, 1977; *Wang and Sheeley*, 1990; *Suzuki*, 2006]. Note that a correlation between W_{hss} and $<n_p>$ is not seen, which one might expect from open-flux expansion-factor arguments; also a correlation between $<n_p>$ and $<v_r>$ is not seen. The familiar strong positive correlation between $<v_r>$ and $<T_p>$ is seen [e.g. *Lopez*, 1987; *Elliott et al.*, 2005; *Borovsky and Steinberg*, 2006]. There are two other significant correlations of note in Table 5. The first is the positive correlation between $<B_{mag}>$ and the heavy-ion charge-state density ratios C^{6+}/C^{4+} and O^{7+}/O^{6+}. The second is the anticorrelation between the iron-to-oxygen abundance ratio Fe/O and $<v_r>$, $|<B_r>|$, and $<n_p>$, which would seem like a correlation that might originate in an open-flux expansion-factor process.

Superposed-epoch analysis is used to determine whether there are any systematic variations with time in the 66 flattop intervals of Table 1. In Figure 3 the superposed epoch averaging is triggered on the onset times chosen for the 66 flattop intervals at 1 AU and in Figure 4 the superposed epoch averaging is triggered on the termination times for the 66 flattop intervals. In the two figures, 30 hr of averaging of the unperturbed coronal-hole plasma is shown: the shortest flattop interval is 22 hr, so after 22 hr the individual flattop events are beginning to drop out of the averaging. At 30 hr, 9 of the 66 events have dropped out of the averaging.

In Figure 3 the superposed averaging of the solar wind quantities for the 66 flattop events at 1 AU is triggered on the start times of the flattop intervals (see Table 1) (with the

start chosen when B_{mag} of the solar wind declines to approximately steady values during the early portion of the flattop). The zero epoch in each panel of Figure 3 is marked with a vertical dashed line. In the top panel the superposed average of the solar wind velocity from the OMNI2 data set is plotted. The superposed average of the solar wind radial velocity is approximately constant after time t=0, with no systematic variation of the solar-wind radial velocity during the flattop. (As will be noted throughout this study, the individual flattop events have variations in the solar-wind velocity so the individual velocity profiles are only approximately flat.) In the second panel of Figure 3 the superposed average of the flow longitude of the solar wind from the OMNI2 data set is plotted. Before time t=0 there is an eastward (positive flow longitude) systematic deflection of the solar wind at the end of the CIR [cf. *Siscoe et al.*, 1969; *Richardson*, 2006]. Time t=0 approximately marks the end of that systematic eastward deflection, and the end of the CIR. In the third panel of Figure 3 the superposed average of 3 plasma parameters from OMNI2 are plotted: the magnetic-field strength B_{mag}, the solar wind proton number density n_p, and the proton specific entropy $S_p = T_p/n_p^{2/3}$. The superposed averages of these three quantities are approximately constant within the unperturbed coronal-hole plasma region after t=0. Note the lower-entropy plasma before the onset of the unperturbed coronal hole region; this low proton entropy is representative of streamer-belt and sector-reversal-region plasma [*Xu and Borovsky*, 2015]. Note also the elevated values of the B_{mag} in the CIR compression before time t=0. Similarly the solar wind number density n_p is elevated before t=0 owing to (a) compression in the CIR and (b) noncompressive density perturbations in the streamer-belt and sector-reversal-region plasmas before the coronal-hole plasma [e.g. *Gosling et al.*, 1981; *Borrini et al.,* 1981]. In the fourth panel of Figure 3 the superposed average of the intensity of the 272-eV electron strahl as measured by ACE SWEPAM is plotted. The intensity of the strahl is notably high in the CIR before t=0, as discussed by *Crooker et al.* [2010].

Note in the fourth panel of Figure 3 that the intensity of the electron strahl systematically decreases with time after t=0 in the unperturbed coronal-hole plasma region. If the coronal-hole plasma is really unperturbed by compression or rarefaction then one might expect the properties of the electron strahl to be uniform in that plasma, with a given flattop interval having a constant expansion factor near the Sun. The reason for the decline in the

superposed average of the strahl intensity is not known: some suggestions are given in the remainder of this paragraph. The rigid rotation of coronal holes versus the differential rotation of the photosphere may play a role in a couple of different ways. First, there is an "age of the coronal-hole floor" issue. At mid latitudes (where coronal hole plasma has its origin for the equatorial heliosphere) the rigid rotation of the coronal hole overtakes the differential rotation of the photosphere, so the photospheric floor is flowing into the coronal hole from the streamer belt on the leading edge of the hole. Hence in going from the westward leading edge of the coronal hole to the eastward trailing edge of the coronal hole, the age of the photospheric floor (how long it has been in the coronal hole) varies, with young floor near the leading edge and old floor near the trailing edge (where the photospheric floor exits the coronal hole). At a latitude of 30° the coronal hole has a synodic period of about 27.5 days and the photosphere has a synodic period of about 28.5 days (cf. Fig. 12 of *Timothy et al.* [1975]). Hence the photosphere flows across the floor of the coronal hole at about 13° of longitude every one solar rotation, which is a speed of about 2.7×10^{-2} km/s. A second difference associated with the coronal hole's rigid rotation is the nature of the interchange reconnection on the leading and trailing edges of the coronal hole, with open flux moving into closed flux (streamer belt) on the leading edge and open flux moving away from closed flux on the trailing edge. This might set up a net gradient in the properties of the open flux across the coronal hole.

In the bottom panel of Figure 3 the superposed averages of some heavy-ion density ratios and charge-state-density ratios are plotted. Before time t=0 a decrease is seen in the O^{7+}/O^{6+}, the C^{6+}/C^{5+}, and the C^{6+}/C^{4+} charge-state ratios as plasma transitions from streamer-belt origin (and sector-reversal-region origin) to coronal-hole origin [cf. *Zhao et al.*, 2009; *Xu and Borovsky*, 2015]. After t=0 in the unperturbed coronal-hole plasma the superposed averages of the O^{7+}/O^{6+}, C^{6+}/C^{5+}, and C^{6+}/C^{4+} charge-state ratios show very slight increases with time (about 10% in the first 24 hours).

In Figure 4 the superposed averaging of the solar-wind quantities for the 66 flattop events is triggered on the end of the flattop intervals (see Table 1) with the end chosen to be the beginning of the systematic decline in the solar-wind radial velocity for each event. The zero epoch in each panel of Figure 4 is marked with a vertical dashed line. In the top panel

the superposed average of the solar wind velocity from the OMNI2 data set is plotted. The superposed average of the solar wind radial velocity is approximately constant before t=0, and the distinct decline in v_r after t=0 is seen. In the second panel of Figure 4 the superposed average of the flow longitude of the solar wind from the OMNI2 data set is plotted. After time t=0 there is an eastward (positive flow longitude) systematic deflection of the solar wind in the beginning portion of the long rarefaction region at the trailing edge of the high-speed stream. (Whereas in the leading-edge compressional CIR the deflection is westward then eastward (negative flow longitude then positive flow longitude), in the trailing-edge rarefaction the deflection is eastward then westward [*Carovillano and Siscoe*, 1969; *Borovsky and Denton*, 2016]. In the third panel of Figure 4 the superposed average of the 3 plasma parameters B_{mag}, n_p, and $S_p = T_p/n_p^{2/3}$ from OMNI2 are plotted. The superposed averages of n_p and B_{mag} show slight systematic decreases with time in the intervals of unperturbed coronal-hole plasma. After the termination of the unperturbed coronal-hole plasma at t=0 the proton-specific entropy declines from high values for coronal-hole-origin plasma to low values for streamer-belt and sector-reversal-region plasma. In the fourth panel of Figure 4 the superposed average of the intensity of the 272-eV electron strahl as measured by ACE SWEPAM is plotted. The intensity of the strahl declines during the unperturbed coronal-hole plasma before t=0 and continues to decline in the trailing edge rarefaction after t=0. In the bottom panel of Figure 4 the superposed averages of some heavy-ion density ratios and charge-state-density ratios are plotted: in the unperturbed coronal-hole plasma before time t=0 the superposed averages of the charge-state ratios are approximately constant and the averages rise after t=0 as a transition from low-charge-state-ratio coronal-hole plasma is made to high-charge-state-ratio streamer-belt and sector-reversal-region plasma.

3.2. Flattop High-Speed Streams in the Inner Heliosphere

Using the Helios 1 and Helios 2 data sets for the inner heliosphere, unperturbed coronal-hole plasma events are chosen similar to the events at 1 AU described in Section 3.1. High-speed streams with flattop velocity profiles are selected, and regions of compression at the leading edges are eliminated and the events are cutoff at the onset of rarefaction at the trailing portions. The inner-magnetosphere unperturbed coronal-hole plasma events are listed

in Table 2. Five events were found in the Helios 1 and 2 data sets, two of which (Flattop Intervals 3 and 4) had very intermittent data coverage and were not used for the analysis in the present report. As noted in Table 2, of the 3 events with good data coverage 2 events were at ~0.3 AU and 1 event was at ~0.6 AU.

In Figure 5 the radial velocity of the solar wind is plotted for the Helios 1 high-speed stream denoted as Flattop Interval 2 in 1975; the interval of unperturbed coronal-hole plasma is marked with the red double arrow.

3.3. Ulysses Polar Crossings

The third collection of unperturbed coronal-hole plasma comes from the polar passes of the Ulysses spacecraft. In Table 3 the 6 polar crossings of Ulysses are listed; in the table the start and end dates denote the beginning and end of the time interval when Ulysses is at a solar latitude greater than 75°. The three southern crossings are each about 85 days long and the three northern crossings are each about 65 days long, with the northern crossings slightly closer to the Sun (~2.0 AU at highest latitude) than the southern crossings (~2.3 AU at highest latitude).

Note the mean solar-wind radial velocities and standard deviations for the six polar crossings in Table 3. For five of the crossings the mean velocities are 730 km/s or higher, but the mean velocity of Polar Crossing 3 in the year 2000 is only 389 km/s. That polar pass contains a lot of slow wind with low proton specific entropy, consistent with streamer-belt plasma rather than coronal-hole plasma. Polar Crossing 4 in the year 2001 also contains clear intervals of slow streamer-belt plasma (and ejecta [*Reisenfeld et al.*, 2003]), though not as much as Polar Crossing 3 does. Both of those crossing occurred during a solar maximum, where the high-latitude fields and plasma are not dominated by polar coronal holes [cf. *McComas et al.*, 2002; *Smith,* 2011]. Polar Crossings 3 and 4 of Table 3 also each contain several intervals of coronal mass ejection (CME) plasma, as cataloged by *Ebert et al.* [2009], *Du et al.* [2010], and *Richardson* [2014]. Ulysses Polar Crossing 5 contains a low-velocity, high-proton-entropy, radial-magnetic-field disturbance from days 36 to 40 of 2007 (at the highest latitude portion of that polar crossing) caused by Ulysses passing through the tail of

comet McNaught [*Neugebauer et al.*, 2007]. Half way through Polar Crossing 6 the time resolution of the data in the Ulysses data set becomes degraded.

In Figure 6 the radial velocity of the solar wind is plotted for the 85-day Polar Crossing 1 (latitude greater than 75°) of the southern polar cap of the Sun. The entire polar crossing contains unperturbed coronal-hole plasma.

4. Plasma Structure in the Unperturbed Coronal Hole Solar Wind

In subsections 4.1 and 4.2 (and in Section 5), the plasma structure of the coronal-hole-origin solar wind will be analyzed. In Section 4.1 the nature of the plasma structure as seen in the solar-wind velocity v_r, in the alpha-to-proton density ratio α/p, in the electron strahl intensity F_e, in the proton specific entropy S_p, in heavy-ion charge-state ratios, etc. is discussed. In Section 4.2 cross correlations between variations in the various plasma measures (v_r, α/p, F_e, S_p, …) in the data from intervals of unperturbed coronal-hole plasma are calculated and discussed.

4.1. Observations of the Plasma Structure

Radial Velocity. In unperturbed coronal-hole plasma at 1 AU the solar-wind radial velocity is characterized by (1) a slower-faster drift of the radial velocity with timescales of several hours to a day and (2) upward spikes of the radial velocity that last a few minutes. The slow-fast drift of the solar-wind velocity is seen by looking at the lower edge of the velocity-versus-time plotted in Figure 1 or in the top panel of Figure 7. That temporal drift in the solar-wind radial velocity is also seen in the Helios observations of the unperturbed coronal-hole plasma at 0.3 AU (cf. Figure 5) and in the Ulysses observations of unperturbed coronal-hole plasma at 2 AU (cf. Figure 6). In the Helios observations of the fast wind such velocity structures were referred to as "flow tubes" [*Thieme et al.*, 1988, 1989] and these velocity structures were suggested to be connected with supergranule structures at the Sun. In Ulysses observations of the fast wind some of this velocity drift has been discussed in terms of "microstreams" [e.g. *Neugebauer et al.*, 1995, 1997]. The upward spikes of radial velocity in the coronal-hole plasma have been noted in the literature as the "one-sided" Alfvenic fluctuations [*Gosling et al.*, 2009] taking the form of "pulses" [*Gosling et al.*, 2011]. (*Gosling*

et al. [2009] note that the one-sided pulses in the solar-wind speed are more prominent when the magnetic field is closer to radial.) Along with the slow drift in the velocity, these upward spikes of radial velocity are seen in the Helios observations at 0.3 and 0.6 AU (see top panel of Figure 8), in Wind and ACE observations at 1 AU, and in the Ulysses observations at ~2 AU (see top panel of Figure 9). When simultaneous Wind and ACE measurements upstream of the Earth are examined, the pulse occurrence is very different at the two spacecraft when the spacecraft are separated by 50 - 100 R_E, indicating that the velocity pulses are localized in spatial extent. In all of these data sets (0.3 AU - 2 AU) the upward spikes of radial velocity are associated with "foldings" or "switchbacks" of the magnetic field wherein the field direction makes very strong deviations (up to 180°) from the Parker-spiral direction. The field foldings are discussed later in this subsection.

Magnetic-Field Strength. The temporal behavior of the magnetic-field strength B_{mag} in the unperturbed coronal-hole plasma at 1 AU is characterized by (1) values of B_{mag} drifting up and down with timescales of ~ 2 hr to ~ 12 hr and (2) localized deep decreases in the values of B_{mag} (magnetic holes [*Turner et al.*, 1977; *Winterhalter et al.*, 2000; *Neugebauer et al.*, 2001]). The temporally drifting values of B_{mag} resemble the temporally drifting values of v_r, but the two quantities do not drift in unison. As was the case for v_r, the magnetic-field strength will sometimes show an abrupt change by 10's of per cent. The magnetic holes have durations of minutes and are often temporally associated with the pulsed increases in the solar-wind radial velocity discussed in the previous paragraph. The pattern of drift of B_{mag} to lower and higher values and the presence of magnetic holes are both seen in all of the unperturbed coronal-hole plasma data sets from 0.3 AU (cf. Figure 8b) to ~2 AU (cf. Figure 9b).

Proton Number Density. The unperturbed coronal-hole plasma at 1 AU is characterized by up and down variations of the proton number density n_p with variation timescales from several hours to about 1 day. In Figure 7c the value of n_p varies by about 50% on these fraction-of-a-day timescales. Similar fraction-of-a-day drifts in the value of n_p are seen at 0.3 AU (Figure 8c) and over the pole at ~2 AU (Figure 9c). There are smaller-scale variations in the number density, some of which may be shot noise in the density measurements. Wind and ACE see different short-timescale variations when the two

spacecraft are separated by 50 - 100 R_E, indicating a spatial localization to the short timescale variations.

Proton Specific Entropy. The proton specific entropy $S_p = T_p/n_p^{2/3}$ in the unperturbed coronal-hole plasma at 1 AU shows variations by about an order of magnitude over timescales of a fraction of a day (cf. Figure 7d). Sometimes the change in S_p occurs abruptly, but more often it is a slow drift in the baseline S_p value. Some of the slow temporal variation in S_p is correlated with temporal variation in the solar-wind radial velocity v_r; sometimes the temporal variabilities of S_p and v_r are independent. Similar temporal variability of S_p is seen in unperturbed coronal-hole plasma at 0.3 AU (Figure 8d) and at ~2 AU (Figure 9d). Shorter-timescale variations are seen that differ on ACE and Wind; some of this is probably localized small-scale variations and some of this is measurement noise.

Helium Abundance. In Figure 7e the alpha-to-proton density ratio α/p is plotted for the unperturbed coronal-hole plasma of Flattop 15 at 1 AU as measured by ACE (black) and Wind (blue); in the hot solar wind at 1 AU the ratio α/p is difficult to measure with an E/q instrument, so data with different instrument types from ACE SWEPAM (an electrostatic analyzer) and from Wind SWE (a Farady cup) are plotted. Also plotted for confirmation of the variations is the 1-hr time-resolution α/p density ratio $\alpha/p = n_\alpha/n_p$ constructed with number density n_α as measured by ACE SWICS using a time-of-flight spectrometer and the number density n_p from ACE SWEPAM. As can be seen in Figure 7c, when there is a large change in the α/p density ratio all three methods agree on the location of the change, but the three methods in general yield different values for α/p. The ratio α/p is not examined in the Helios data set since close to the Sun the temperatures of the protons and alpha particles are even hotter. Ulysses at 2 AU has cooler ion populations, so alpha particles and protons are more-easily separated for analysis; here (cf. Figure 9e) the ratio α/p is examined. The α/p density ratio shows variability by ~50% in the fraction-of-a-day timescale in unperturbed coronal-hole plasma at 1 AU (cf. Figure 7e) and at 2 AU (cf. Figure 9e). The density ratio α/p sometimes shows abrupt strong transitions within unperturbed coronal-hole plasma: an example of that is seen at t = 309.673 in Figure 7e, where a transitional increase by almost a factor of 2 occurs in about 2 minutes. Very rapid (few-second) transitions in the helium

abundance α/p in the solar wind at 1 AU are common [cf. *Sarfankova et al.*, 2013; *Zastenker et al.*, 2014].

Electron Strahl. It is well known that coronal-hole plasma (high-speed solar wind) characteristically has a narrow, robust, unidirectional electron strahl [cf. *Feldman et al.*, 1978; *Fitzenreiter et al.*, 1998; *Hammond et al.*, 1996], with noted temporal variability in the measured strahl flux [cf. *Gosling et al.*, 2004; *Louarn et al.*, 2009]. Figure 7 plots the phase-space density f_{272} (in units of s^2cm^{-5}) of the electron strahl in the field-aligned (antisunward) direction at an energy of 272 eV, as measured by ACE SWEPAM. The black curve is a 20-minute running average of the value of f_{272} and the red curve is a 2-hr running average of the value of f_{272}. Considerable high-frequency variability can be seen in the 20-minute-averaged black curve, and longer-time trends in the strahl intensity can be seen in the 2-hr-averaged red curve. These longer-time trends can be described as fraction-of-a-day changes in the strahl intensity by factors of 2 to 4.

Heavy Ions. In Figure 7g three charge-state density ratios O^{7+}/O^{6+}, the C^{6+}/C^{5+}, and the C^{6+}/C^{4+} and the iron-to-oxygen density ratio Fe/O are plotted for the unperturbed coronal-hole plasma of Flattop 15 as measured by ACE SWICS with 1-hr time resolution. Although the ratios do not show much variability in Figure 7g, for most intervals of unperturbed coronal-hole plasma examined at 1 AU the variability can be considerable, often with transitions in the ratios by fractions of a decade.

Magnetic-Field Foldings. Localized magnetic-field foldings (magnetic switchbacks, field reversals) are well known in the coronal-hole plasma of the Ulysses polar-crossing data set [e.g. *Balogh et al.*, 1999; *Yamauchi et al.*, 2004; *Neugebauer and Goldstein*, 2013]. They are also seen in the coronal-hole plasma at 1 AU [e.g. *Kahler et al.*, 1996] and at 0.3 AU. In the top panel of Figure 10 the solar-wind radial velocity in unperturbed coronal-hole plasma (Flattop 5) as measured by ACE at 1 AU is plotted as the black curve and in the bottom panel $\underline{b} \bullet \underline{n}_{ps}$ is plotted in black as measured by ACE. Here, $\underline{b} = \underline{B}/B_{mag}$ is the unit vector direction of the measured magnetic field and $\underline{n}_{ps}$ is the unit vector of the calculated Parker-spiral direction. When $\underline{b} \bullet \underline{n}_{ps} = 1$ the field is exactly in the direction of the Parker spiral and when $\underline{b} \bullet \underline{n}_{ps} = -1$ it is exactly reversed. In the bottom panel of Figure 10 several examples of localized strong deviations of the magnetic-field direction from the Parker-spiral direction are indicated with

the blue letters. As seen in the top panel, those field deviations from the Parker spiral are associated with localized increases in the solar-wind radial velocity, the "one-sided" Alfvenic fluctuations [*Gosling et al.*, 2009] taking the form of "pulses" [*Gosling et al.*, 2011] that were noted above in the discussion of velocity structure. Plotted in red in the two panels of Figure 10 are higher-time-resolution (3-s) measurements by Wind. In RTN coordinates ACE and Wind were separated by about 70 R_E in the T-N plane with Wind about 120 R_E downstream from ACE in the R direction. Note the difference in the pattern of velocity pulses seen by the two spacecraft and the difference in the pattern of field foldings; this difference indicates that the spatial structure of the velocity pulses and field foldings in the unperturbed coronal-hole plasma is quite limited, probably on the order of 10's of R_E in scale. Note also in the red curves of Figure 10 that very brief pulses and foldings are seen in the higher-resolution Wind measurements. In Figure 11 the solar-wind velocity (top panel) and $\underline{b}\bullet\underline{n}_{ps}$ (bottom panel) are plotted in unperturbed coronal-hole plasma at 0.31 AU as measured by Helios 1 in Flattop 2. A number of isolated field foldings are denoted by the blue letters in the bottom panel, and their accompanying radial velocity pulses are seen in the top panel. In Figure 12 the solar-wind velocity (top panel) and $\underline{b}\bullet\underline{n}_{ps}$ (bottom panel) are plotted in unperturbed coronal-hole plasma at 2.3 AU as measured by Ulysses in Polar Crossing 1. A number of localized field reversals are denoted by the blue letters in the bottom panel and their accompanying radial velocity pulses are seen in the top panel. Note that it is more difficult to isolate the field reversals and the radial velocity pulses in Figure 12 at 2.3 AU than it was in Figures 10 and 11 closer to the Sun. The lower time resolution (4-min) of the plasma instrument on Ulysses may be part of the difficulty. In Figure 13 the quantity $\underline{b}\bullet\underline{n}_{ps}$ is binned for the various collections of unperturbed coronal-hole plasma. In the three curves in the top panel of Figure 13 $\underline{b}\bullet\underline{n}_{ps}$ is binned individually for Helios measurements in three flattop intervals from Table 2. The red curve is at ~0.6 AU and the green and blue curves are at ~0.3 AU. In the second panel of Figure 13 $\underline{b}\bullet\underline{n}_{ps}$ is binned individually for ACE measurements in a sampling of 8 flattop intervals from Table 1. All curves are at 1 AU. Comparing the top and second panels, it is seen that the distribution of $\underline{b}\bullet\underline{n}_{ps}$ values is evolving away from $\underline{b}\bullet\underline{n}_{ps} = 1$ with distance from the Sun. In the four curves in the third panel of Figure 13 $\underline{b}\bullet\underline{n}_{ps}$ is binned individually for Ulysses measurements in four polar crossings from Table 3: Polar Crossings 3 and 4 at

solar maximum are not used and 7 days of data are cleaned from Polar Crossing 5 to eliminate the encounter with comet McNaught. In the bottom panel of Figure 13 the averages of the $\underline{b} \bullet \underline{n}_{ps}$ binnings at the various distances from the Sun are plotted: the red curve is Helios at ~0.3 AU, the orange curve is Helios at ~0.6 AU, the green curve is ACE at 1 AU, and the blue curve is Ulysses at ~2 AU. The evolution with distance from the Sun of the distribution of $\underline{b} \bullet \underline{n}_{ps}$ values from +1 is clearly seen in these four curves (see also Fig. 14 of *Borovsky* [2010]): there is more deviation from the Parker-spiral direction with distance from the Sun in the unperturbed coronal-hole plasma.

Alfvenicity. In the Alfvenic solar wind there are temporal correlations between the vectors $\underline{v}$ and $\underline{B}$, or more precisely, between the vectors $\underline{v}$ and $\underline{v}_A$ where $\underline{v}_A = \underline{B}/(4\pi m_p n_p)^{1/2}$. In the solar-wind plasma these correlations are patchy in the sense that the functional relation between $\underline{v}(t)$ and $\underline{v}_A(t)$ changes with time. In Figure 14 a plot of the radial component of the magnetic-field vector in Alfven units $v_{Ar} = B_r/(4\pi m_p n_p)^{1/2}$ vertically versus the radial component of the plasma flow vector v_r horizontally is made for the entire interval of unperturbed coronal-hole plasma of Flattop 15 (see Table 1) as measured by ACE at 1 AU. The temporal sequence of points $v_{Ar}(t)$ versus $v_r(t)$ moves back and forth along a line in v_{Ar}-v_r space, and then there is a sudden jump wherein the $v_{Ar}(t)$-versus-$v_r(t)$ sequence of points moves back and forth along another line in v_{Ar}-v_r space. In the top panel of Figure 14, for the temporal sequence of Flattop 15 the color of the plotted points is changed every time the v_{Ar}-versus-v_A pattern shifts to a new line; 13 sub-intervals are found plotted by the 13 different colors. For each of the 13 sub-intervals, the Pearson linear correlation coefficient R_{corr} is listed on the top panel: the 13 correlation coefficients vary from 86% to 98%. Each subinterval is highly Alfvenic. However, the transitions from one subinterval to another are not very Alfvenic. If the correlation coefficient between v_{Ar} and v_r is calculated for the entire Flattop 15 interval the coefficient 31% is obtained, much lower than the coefficient for an individual Alfvenic subinterval. From an Alfvenicity point of view, the unperturbed coronal-hole plasma is spatially structured with blocks of highly Alfvenic plasma and transitions that are not very Alfvenic. In the bottom panel of Figure 14 the radial velocity of the solar wind v_r is plotted for the entire interval of Flattop 15, with the color of the plotted points changing according to which Alfvenic subinterval the spacecraft is within. In Flattop 14 at 1 AU, 13

subintervals of plasma are observed in 71 hours of spacecraft measurements. A similar analysis of the Helios 1 measurements in Flattop Interval 2 at 0.31 AU (cf. Table 2) finds 10 subintervals of data in 58 hours of measurements. These subintervals of highly Alfvenic behavior are indicators of a structuring of the coronal-hole plasma.

4.2. Correlations in the Unperturbed Coronal-Hole Plasma

Table 6 contains Pearson linear correlation coefficients for unperturbed coronal-hole plasma at 1 AU and Table 7 contains Pearson linear correlation coefficients for unperturbed coronal-hole plasma at ~2 AU. The data utilized to calculate the correlations of Table 6 is all of the available data for the 66 flattop intervals of Table 1. The data utilized to calculate the correlations of Table 7 are the data from Ulysses Polar Crossings 1, 2, 5, and 6 with Polar Crossing 5 cleaned to eliminate the interval wherein Ulysses encounters the tail of comet McNaught. Polar Crossings 3 and 4 at solar maximum were not used since those intervals are poorly representative of unperturbed coronal-hole plasma.

Correlation coefficients between two quantities are indications of how much the variances of one quantity are described by the variances of the other quantity. In Tables 6 and 7 the correlation coefficients are driven by variations from one interval to another and by variations within the intervals. (The coefficients in Table 5 are only driven by variations between intervals.)

Examining the coefficients for unperturbed coronal-hole plasma at 1 AU in Table 6, some of the correlations are familiar and some are not. One familiar set of correlations in Table 6 are the strong positive correlations between v_r, S_p, and T_p [e.g. *Lopez,* 1987; *Burlaga et al.*, 1990; *Elliott et al.*, 2005; *Borovsky*, 2012c]. Another familiar set of correlations is the anticorrelation between the solar wind radial velocity v_r and the heavy-ion charge-state ratios O^{7+}/O^{6+} and C^{6+}/C^{5+} [e.g. *Gloeckler et al.*, 2003], although the anticorrelations for unperturbed coronal-hole plasma in Table 6 are not nearly as strong as the anticorrelations when all types of solar wind are mixed (as in Table 2 of *Borovsky* [2012c] or Fig. 2 of *Xu and Borovsky* [2015]). Note in Table 6 that the proton specific entropy S_p is basically uncorrelated with the heavy-ion charge-state ratios O^{7+}/O^{6+} and C^{6+}/C^{5+} for unperturbed coronal-hole plasma at 1 AU; this is in stark contrast to the very strong anticorrelations between S_p and the

ratios O^{7+}/O^{6+} and C^{6+}/C^{5+} at 1 AU when all types of solar-wind plasma are used for the correlations (cf. Tables 1-4 of *Pagel et al.* [2004], Table 2 of *Borovsky* [2012c], or Fig. 9 of *Xu and Borovsky* [2015]). Another familiar correlation in Table 6 is the positive correlation between the intensity of the electron strahl f_{272} and the magnetic-field strength B_{mag} [cf. *Feldman et al.*, 1976b; *Scime et al.*, 1994; *Crooker et al.*, 2010]. Note that the strahl intensity f_{272} also shows positive correlations with the heavy-ion charge-state ratios O^{7+}/O^{6+}, C^{6+}/C^{5+}, and C^{6+}/C^{+} in Table 6: since higher charge-state ratios are caused by higher corona electron temperatures [cf. Fig 2 of *Landi et al.*, 2012], this positive correlation may be an indication of more-robust electron strahl from regions of the corona that have higher electron temperatures. Another correlation of note in Table 6 is the negative correlation between the alpha-to-proton density ratio α/p and the value of B_{mag}/n_p in the plasma. Note in Table 6 that the iron-to-oxygen density ratio Fe/O of the unperturbed coronal-hole plasma at 1 AU is not strongly correlated with other solar-wind parameters.

In Table 7 the coefficients for unperturbed coronal-hole plasma in the polar crossings ($>75^o$ latitude) of Ulysses are displayed. Since the Ulysses spacecraft varies in distance from the Sun during those crossings, distance-normalized variables such as $B_{mag}r^2$, n_pr^2, and v_Ar are used in the correlations. In Table 7 the familiar positive correlations between v_r, S_p, and T_p are seen, although the correlations may be weaker than found at 1 AU in Table 6. (It is difficult to directly compare correlation coefficients obtained in different data sets, like Table 6 versus Table 7.) Weaker correlation may have to do with cumulative in situ heating of the protons in the coronal-hole-origin solar wind [cf. *Schwenn et al.*, 1981; *Freeman and Lopez*, 1985; *Hellinger et al.*, 2011; *Borovsky and Gary*, 2014]. In Table 7 the positive correlation between S_p and v_A is also seen, but again apparently weaker than at 1 AU in Table 6. In Table 7 the Ulysses polar-crossing data shows a positive correlation between the alpha-to-proton density ratio and S_p that is not seen at 1 AU in Table 6: this positive correlation further from the Sun may represent cumulative heating of the coronal-hole-origin solar-wind protons by alpha particles with more proton heating (higher S_p) associated with higher fractional densities of alphas [cf. *Schwartz et al.*, 1981; *Sarfrankova et al.*, 2013; *Borovsky and Gary*, 2014].

5. Examining the Solar-Wind Data in Terms of Movement along the Photosphere

To discern whether there are characteristic structure sizes in the coronal-hole plasma that might have origins at the Sun, in this section the time-series measurements of the solar wind from the various spacecraft are converted from progressing time to progressing distance along the photosphere.

5.1. Converting Spacecraft Time into Photospheric Distance

To do this conversion, estimates of the solar-wind-origin foot-point velocity v_{photo} of the spacecraft along the photospheric floors of the coronal holes must be obtained. With this photospheric velocity v_{photo}, time t in the spacecraft measurements is converted to distance d along the photosphere via the expression $d = v_{photo}t$. This conversion assumes that the foot-point motion on the Sun is smooth, whereas in reality the open-flux mapping foot point of a heliospheric spacecraft jumps from flux tube to flux tube into the solar surface (e.g. from funnel to funnel), with these open flux tubes mostly residing on the supergranule boundaries.

Estimating the foot point velocity v_{photo} is easiest for the high-latitude polar crossings of Ulysses. Here the origin point of the solar wind resides deep within a polar coronal hole where the open flux is nearly radial and the solar-wind plasma undergoes a uniform expansion factor (radial expansion) near the Sun throughout the polar crossing. Hence, the nadir point of the spacecraft is approximately the solar-wind-origin footpoint, with a time lag owing to the advection of the solar wind from the Sun to Ulysses. At a latitude of θ_{lat} the Ulysses nadir point on the Sun makes a circular path that is $2\pi r_s \cos(\theta_{lat})$ in length every solar rotation, with the solar radius $r_s = 7 \times 10^5$ km. With a high-latitude rotation rate of about 35 days, at $\theta_{lat} = 80°$ the foot-point velocity is $v_{photo} = v_{nadir} = 0.25$ km/s = 22000 km/day. These values are entered into Table 8.

In the equatorial regions the solar-wind-origin footpoint motion is more complicated owing to the super-radial expansion of coronal-hole plasma away from the Sun. With an equatorial rotation period of about 27 days, the Earth's nadir point moves along the photosphere of the Sun with a velocity of about $v_{nadir} = 1.9$ km/s. The solar-wind origin point,

however is not the nadir point. Rather the origin footpoint moves along the floor of coronal-hole regions that are typically not on the solar equator and then the footpoint jumps a large distance from one coronal-hole region into another coronal-hole region [cf. *Leamon and McIntosh*, 2009]. Owing to the expansion of open flux coming out of the low-latitude coronal-hole regions the solar-wind origin footpoint moves slower than 1.9 km/s across the floor of the hole and moves much faster than 1.9 km/s when it is making a jump. The motion across the floor is of interest for the present study. Examination of several of the unperturbed-coronal-hole-plasma intervals in Table 1 with the Wang-Sheeley-Arge mapping of the Earth's solar-wind-origin footpoint [*Arge et al.*, 2003] (courtesy of Nick Arge, 2009) finds photospheric velocities of the Earth's solar-wind-origin footpoint being in the range of 0.15 - 1 km/s on the coronal-hole floors of Table 1. In Figure 15 the footpoint velocity on the photosphere of the Earth's solar-wind-origin footpoint calculated with WSA is binned for the declining-phase years 2004-2008. The occurrence distribution in Figure 15 has two parts, a low-velocity hump and a high-velocity tail; one interpretation is that the hump part of the distribution represents the velocity of the footpoint on the floors of coronal holes and that the high-velocity tail represents jumps across streamer-belt regions from one coronal-hole region into another. The median value for the years 2004-2008 is 0.51 km/s; from this, the value $v_{photo} = 0.5$ km/s will be taken as a typical velocity of the solar-wind-origin footpoint across the photosphere for the unperturbed coronal-hole plasma intervals at 1 AU (cf. Table 1). This value is about 1/4 of the value of the nadir velocity v_{nadir}. These values are entered into Table 8.

The orbital ephemeris in the Helios 1+2 data sets indicates that for the fast-moving Helios 1+2 spacecraft, the nadir point of the spacecraft moves at $v_{nadir} \sim 1.8$ km/s across the photosphere for Flattop Interval 1 (Helios 1) at 0.61 - 0.67 AU, the nadir point moves at $v_{nadir} \sim 1.0$ km/s in the photosphere for Flattop Interval 2 (Helios 1) at 0.31 AU, and the nadir point moves at $v_{nadir} \sim 0.94$ km/s for Flattop Interval 5 (Helios 2) at 0.29 - 0.31 AU. As is the case for ACE and Wind in the ecliptic plane at 1 AU, the solar-wind-origin footpoint of the Helios spacecraft near the ecliptic plane probably moves a factor of four slower across the coronal-hole floor owing to the expansion of the open flux from coronal holes into the equatorial heliosphere. With the rough estimate obtained from WSA at Earth that v_{photo} for the floor of a

coronal hole is about 1/4 the nadir velocity v_{nadir}, the footpoint velocity $v_{photo} = 0.45$km/s is taken for the Helios Flattop Interval 1 and $v_{photo} = 0.25$ km/s is taken for the Helios Flattop Intervals 2 and 5. These values are entered into Table 8.

A typical supergranule size on the photosphere is $\sim 3 \times 10^4$ km [e.g. *Simon and Leighton*, 1964; *Hagenaar et al.*, 1997; *Srikanth et al.*, 2000], which is about 1/150 times the equatorial circumference of the Sun. In Table 8 the approximate supergranule crossing times $\tau_{super} = (30000 \text{ km})/v_{photo}$ for the spacecraft footpoints moving along the floors of coronal holes at a speed of v_{photo} are tabulated.

5.2 Structure in the Solar-Wind Plasma from Coronal Holes

Using the estimates of v_{photo} in Table 8 to convert the spacecraft time series into distance along the photosphere, the spacecraft measurements of structure in the unperturbed coronal-hole plasma at different distances from the Sun are compared in Figures 16-21. The curves plotted in those figures are all 1.5-hr running medians of the spacecraft measurements (85-point medians for the 64-s-resolution ACE measurements, 23-point medians for the 4-min-resolution Ulysses plasma measurements, 90-point medians for the 1-min-resolution Ulysses magnetic-field measurements, and 135 point medians for the 40-s-resolution Helios measurements). The running median is chosen as a method to de-spike the data [*Nodes and Gallagher*, 1982]. A running medium of 1.5-hr width corresponds to approximately 1350 km in the Ulysses curves and the Helios 0.3-AU curves and corresponds to approximately 2700 km in the ACE curves and the Helios 0.6 AU curve.

Magnetic-Field Strength. In the top panel of Figure 16 the magnetic-field strength B_{mag} measured in the solar wind is plotted logarithmically as a function of approximate distance along the photosphere for Ulysses measurements in Polar Crossings 1 and 2 (red and orange curves), for ACE measurements in Flattop Intervals 5, 15, 25, 33, and 39 (green-blue-purple curves), for Helios 1 measurements at 0.6 AU in Flattop Interval 1 (light blue curve), and for Helios 1 + 2 measurements at 0.3 AU in Flattop Intervals 2 and 5 (black and gray curves). In the top panel of Figure 16 the approximate $B_{mag} \propto r^{-2}$ (purely radial field) to $B_{mag} \propto r^{-1}$ (purely transverse-to-radial field) expansion of the solar wind is clearly seen with B_{mag} being about a factor of 40 times weaker for the Ulysses curves at ~2.3 AU than for the Helios

curves at 0.3 AU. The approximate size of a 30000-km diameter supergranule is indicated on the plot by the red double arrow. The various curves in the top panel of Figure 16 show variations in B_{mag} with relative amplitudes of slightly less than a factor of 2 with several variations per supergranule scale size.

Proton Number Density. In the bottom panel of Figure 16 the proton number density n_p of the coronal-hole-origin solar wind is plotted logarithmically as a function of the approximate distance along the photosphere. The color codings of the curves are labeled on the plot (same scheme as in the top panel) and the size of a 30000-km supergranule is indicated by the red double arrow. The $n_p \propto r^{-2}$ decrease in density with distance r is clearly seen with the average densities at 0.3 AU being a factor of about 60 times the average densities at ~2.3 AU. In all curves a variability in the proton density by factors of 2 or less are seen, with several variations per supergranule size in all curves. In no case is the coronal-hole plasma homogeneous.

B_{mag}/n_p. The quantity B_{mag}/n_p is of particular interest because this quantity does not change under the action of compression and rarefaction transverse to the magnetic field, nor does it change under the action of adiabatic or non-adiabatic heating or cooling. In Figure 17 B_{mag}/n_p is plotted logarithmically as a function of the approximate distance along the photosphere. Since $n_p \propto r^{-2}$ and approximately $B_{mag} \propto r^{-2}$ (the latter being approximately true for fast wind in the ecliptic at 1 AU), there is not a strong variation in B_{mag}/n_p with distance from the Sun. Since B_{mag}/n_p is impervious to compression, expansion, and heating, it is a robust quantity to use to compare structure scale sizes at different distances from the Sun. In Figure 17 the spacecraft measurements of B_{mag}/n_p are plotted for about 1 supergranule diameter of measurements. Relative variations of B_{mag}/n_p by a factor of 2 or less are seen in the various spacecraft curves, with several variations per supergranule in each curve. There is no obvious trend in the characteristic scale sizes of structure from 0.3 AU (black and gray curves) to ~2 AU (red and orange curves), or for the other curves in between at 0.6 AU and 1 AU.

Proton Specific Entropy. In Figure 18 the proton specific entropy $S_p = T_p/n_p^{2/3}$ is plotted logarithmically as a function of approximate distance along the photosphere. The proton specific entropy is invariant to adiabatic compressions and expansions of the plasma,

but is a measure of the amount of nonadiabatic proton heating that the plasma has undergone. It is well known that the protons of the fast wind are nonadiabatically heated with distance from the Sun, which produces a temperature decrease with distance that is slower than the decrease associated with pure adiabatic expansion [cf. *Schwenn et al.*, 1981; *Freeman and Lopez*, 1985; *Hellinger et al.*, 2011; *Borovsky and Gary*, 2014]. Figure 18 shows the progression of the increase in proton specific entropy from 0.3 AU (black and gray curves), to 0.6 AU (light-blue curve), to 1 AU (multiple blue, green, and purple curves), to ~2 AU (orange and red curves). The average proton specific entropy at ~2 AU is about a factor of 160 time greater than the average at 0.3 AU. It is also seen that the relative amplitude of variations of S_p decrease with distance from the Sun: the variation amplitude in the 0.3-AU curves is about a factor of about 4, while the variation amplitude in the ~2-AU curves is about a factor of 1.5. This reduction in the relative amplitude may indicate that the proton heating that gave rise to the entropy increase is a bulk heating throughout the plasma (see also Figure 19) with the mean temperature rising while temperature spatial variations are not effected. For each of the S_p curves in Figure 18, there are several variations per supergranule scale size.

Proton Temperature. In Figure 19 the proton temperature T_p is plotted logarithmically as a function of approximate distance along the photosphere for the Helios measurements at 0.3 AU (black and gray curves) and for the Ulysses measurements at ~2 AU (red and orange curves). The proton temperature at ~2 AU is cooler than the temperature at 0.3 AU owing to adiabatic cooling by the solar-wind expansion being greater than nonadiabatic proton heating (cf. Fig 2 of *Borovsky and Gary* [2014]). The relative amplitude of the temperature variations are greatly reduced from a factor of more than 4 at 0.3 AU to a factor of about 1.5 at ~2 AU. This is indicative of a distributed heating of the plasma that raises the bulk temperature everywhere and so reduces the relative amplitude of the initial variations in temperature. Of course, the temperature is actually cooler at ~2 AU because of the action of adiabatic cooling which is greater than the action of the uniform heating.

Helium Abundance. In Figure 20 the alpha-to-proton density ratio α/p is plotted linearly as a function of approximate distance along the photosphere for the Ulysses Polar Crossings 1 and 2 (red and orange curves). (The α/p ratios at 1 AU are deemed inaccurate

and are not utilized here: ACE SWEPAM, Wind SWE, and the ACE SWICS/SWEPAM combination all yield α/p values that vary considerably from 1% to 8% in the coronal-hole plasma with values that do not agree between the three measures.) The α/p density ratio is invariant to compression and decompression of the plasma and is invariant to any non-adiabatic heating of the protons or alpha particles. Figure 20 shows variations in α/p by about a factor of 2, with several variations per supergranule scale size.

Solar-Wind Radial Velocity. The structure of the solar-wind radial velocity in coronal-hole-origin solar wind is examined in Figures 21 and 22. In the top panel of Figure 21 the radial velocity of the solar wind is plotted linearly from two intervals of unperturbed coronal-hole plasma at 0.3 AU (black and gray curves) and from two intervals at ~2 AU (red and orange curves). The approximate size of a supergranule is denoted by the red double arrow: in all of the curves several variations per supergranule scale size are seen. The amplitude of the velocity variations is larger at 0.3 AU than it is at ~2 AU. The 0.3-AU Helios 1 measurements in Flattop Interval 2 are replotted in black in Figure 22; using the technique of *Thieme et al.* [1989] the Alfvenic fluctuations are subtracted off of the black curve and the result is plotted in red in Figure 22. The subtraction takes the measured proton velocity v_r and produces a "corrected" proton velocity v_{rc} according to $v_{rc} = v_r \pm v_{Ar}$, where v_{Ar} is the velocity of the r-component Alfvenic fluctuation $v_{Ar} = \Delta B_r/(4\pi m_p n_p)^{1/2}$ where the magnetic-field fluctuation $\Delta B_r = B_r - <B_r>$, with B_r being the instantaneous value of B_r and $<B_r>$ being a time average of B_r. Depending on the length of the time averaging, Alfven waves of different scales are subtracted. For the red curve in Figure 22 a 501-point (3.3-hr) running average is used as the baseline $<B_r>$, so Alfvenic fluctuations with timescales of about 3.3-hr or shorter are subtracted off the black curve to make the red curve. As seen, most of the strong fluctuations of the black curve in Figure 22 (and in the top panel of Figure 21) are subtracted off; hence those strong fluctuations were Alfvenic fluctuations. If a longer-time running average were taken for a baseline, longer-timescale Alfvenic fluctuations would be subtracted off; it has been noted in the literature that the large-spatial-scale (low-frequency) velocity fluctuations of the solar wind are Alfvenic [cf. *Bruno et al.*, 1985; *Roberts et al.,* 1987; *Bavassano and Bruno*, 1992]. But not all of the low-frequency fluctuations of v_r are Alfvenic; it has been noted in Section 4.1 (cf. Figure 14) that there are non-Alfvenic transitions of v_r

between Alfvenic patches of the coronal-hole plasma. The variations in the two Ulysses curves of the top panel of Figure 21 are also very Alfvenic, as determined by the strong local correlations between v_r and B_r; however (for some reason) the *Thieme et al.* [1989] $v_{rc} = v_r \pm v_{Ar}$ technique is not successful at cleanly subtracting off the Alfvenic fluctuations in those Ulysses curves. Perhaps the amplitudes of the variations are too small in comparison with the accuracies of measurements of n_p (used in the denominator of the Alfven speed) for the subtraction technique to be of low noise. The top panel of Figure 21 shows several variations per supergranule scale for the solar-wind radial velocity at both 0.3 AU and at ~2 AU. Much of the variability of v_r is Alfvenic, and Alfvenic fluctuations are limited in amplitude to $\pm v_A$; since the Alfven speed v_A of the solar-wind plasma decreases with distance r from the Sun, it is only natural that the amplitudes of Alfvenic variations of v_r decrease with distance from the Sun in the top panel of Figure 21. It may be that the Alfvenic variations in v_r at Ulysses are limited by the lower Alfven speed there. The mean Alfven speed for Polar Crossings 1 and 2 is 44 km/s, which is more than half the size of the peak-to-peak amplitudes of the variations in the Ulysses red and orange curves. The Helios gray and Black curves have amplitudes about twice the Ulysses amplitudes. In the bottom panel of Figure 21 the measurements of the solar-wind radial velocity in the 5 intervals of unperturbed coronal-hole plasma at 1 AU are plotted as a function of the approximate distance along the photosphere. Again, several variations of v_r per supergranule are seen: again some of the variations are Alfvenic and some are not.

6. Summary Assessment of the Structure in Coronal-Hole-Origin Solar Wind

An assessment of the observations of structure in the unperturbed coronal-hole plasma is as follows.

(1) Structure in the coronal-hole-origin solar wind is seen in all measured quantities.

(2) The structure amplitudes are factors of two for the magnetic-field strength B_{mag}, the proton number density n_p, the ratio B_{mag}/n_p, and the α/p density ratio. The amplitudes do not vary significantly with distance from the Sun.

(3) As the proton specific entropy increases systematically from the Sun, the relative amplitude of the structure variations decrease. Similarly the relative amplitude of the

structure variations of the proton temperature decrease with distance from the Sun. A non-adiabatic proton heating with distance uniformly throughout the solar-wind plasma may be the cause of this reduction in amplitude.

(4) The amplitude of variations in the solar-wind radial velocity decrease with distance from the Sun. Since most of the radial velocity variations are Alfvenic and limited to the Alfven speed, and since the Alfven speed decreases with distance from the Sun, it is not unexpected that the amplitudes of radial velocity variations decrease.

(5) Variability in the electron strahl by factors of 2 to 4 are seen, as measured at 1 AU by the amplitude of the phase-space distribution function at 272-eV.

(6) In all measured quantities, several variations per supergranule scale size are observed. The scale size of structure in the coronal-hole-origin solar wind seems to be a fraction of the supergranule scale.

(7) No systematic evolution of the structure scale size is observed with distance from the Sun, over the range 0.3 AU to ~2.3 AU. This is consistent with relic structure from the Sun being advected outward without destruction.

(8) In Section 7 it is argued quantitatively that the observed structure scales in the solar wind are consistent with the production of plasma from open-flux funnels in coronal holes.

(9) The population of magnetic-field foldings (reversals, switchbacks) associated with Alfvenic velocity pulses evolves with distance from the Sun. The magnetic field is mostly Parker-spiral aligned at 0.3 AU and becomes more and more misaligned with distance outward.

7. Discussion: Expectations for Structure Scales

To estimate expected structure scale sizes in the coronal-hole-origin solar-wind plasma, (1) the birth of solar wind in open-flux funnels in coronal holes is considered and (2) the reducing action of eddy diffusion in turbulence in the solar-wind plasma is considered.

7.1. Solar Wind Emanating from Coronal Holes

In the inner heliosphere 10's of solar radii from the Sun field-aligned density structures (polar plumes) connected to coronal holes are imaged that are supergranule size in diameter [*Fisher and Guhathakurta*, 1995; *Woo*, 1996; *DeForest et al.*, 1997; *Woo and Habbal*, 1997] and radio scintillation detects much-smaller-scale density perturbations in the coronal-hole solar wind away from the Sun [*Woo*, 2006].

For solar-wind plasma emanating from coronal holes the expected structure size can be estimated as follows. For conceptual simplicity, the approximation is taken that the entire solar surface is covered with a single coronal hole with uniformly expanding (radially expanding) solar wind; in the end this uniformity assumption will only be exploited for a fraction of the solar surface such as the center of a polar coronal hole.

The total open flux F_{sw} in the solar wind at a distance r from the Sun is

$$F_{sw} \; = \; 4\pi r^2 <B_r> \tag{1}$$

where $<B_r>$ is an average of the (signed) radial component of the magnetic field in the solar wind. The signed value B_r is averaged rather than the absolute value of B_r to reduce the effect of magnetic-field foldings (switchbacks) [*Kahler et al.*, 1996; *Balogh et al.*, 1999] in the coronal-hole-origin plasma. The quantity $<B_r>r^2$ is obtained from the Ulysses polar crossings (cf. Table 3) where the expansion of the solar wind near the Sun should not be super-radial; the values obtained are $<B_r>r^2 = -3.1$ nT AU^2 from the Ulysses Polar Crossing 1, $<B_r>r^2 = +2.8$ nT AU^2 from Polar Crossing 2, and $<B_r>r^2 = +2.4$ nT AU^2 from Polar Crossing 5 (cleaned to remove the encounter with comet McNaught). Taking $<B_r>r^2 \approx 2.8$ nT AU^2, expression (1) yields (with 1 nT = 10^{-5} G and 1 AU = 1.5×10^8 km) $F_{sw} = 7.92\times10^{12}$ G km^2 for the total open flux in the heliosphere (for this single-coronal-hole picture). It is believed that the coronal-hole open flux originates at the photosphere in magnetic funnels that reside within the magnetic network lanes at the boundaries of supergranules [*Dowdy et al.*, 1987; *Tu et al.*, 2005; *Peter,* 2007; *Kayshap et al.*, 2015]. A magnetic-funnel base in the photosphere is seen as a G-band (4305 Å) bright point (magnetic bright point, network bright point) [*Ishikawa et al.*, 2007; *Cranmer,* 2009]. If there are N_{funnel} funnels of open flux on the coronal-hole-covered Sun, then the total open flux produced at the Sun by the open funnels is

$$F_{sun} \; = \; N_{funnel} \, d_{bp}^{\;2} \, B_{bp} \quad , \tag{2}$$

where d_{bp} is the diameter of a bright point (funnel base) and B_{bp} is the magnetic-field strength in the bright point. Typical values are $d_{bp} \sim 150$ km [*Utz et al.*, 2013; *Yang et al.*, 2014] and $B_{bp} \sim 1500$ G [*Ishikawa et al.*, 2007; *Criscuoli and Uitenbroek*, 2014]; with those two parameters, expression (2) yields $F_{sun} = N_{funnel} \, 3.38 \times 10^7$ G km^2 for the total open flux coming out of the funnels. Equating the two above expressions $F_{sw} = F_{sun}$ yields $N_{funnel} = 2.34 \times 10^5$ for the number of funnels required to yield the heliospheric total open flux (if the whole sun was covered by a single coronal hole).

The diameter d_{super} of a supergranule on the photosphere is about 30000 km [e.g. *Simon and Leighton*, 1964; *Hagenaar et al.*, 1997 *Srikanth et al.*, 2000]; hence a single supergranule has an area $A_{super} = d_{super}^2 = 9 \times 10^8$ km^2 on the photosphere. The Sun has a total surface area of $A_{sun} = 6.15 \times 10^{12}$ km^2; hence there are about $N_{super} = A_{sun}/A_{super} = 6830$ supergranules covering the solar surface. The number of funnels per supergranule n_{funnel} is

$$n_{funnel} = N_{funnel}/N_{super} = 34.2 \tag{3}$$

So (for the single-coronal-hole approximation we have been making), for large coronal holes with "radial" expansion of the solar wind, the average number of funnels per supergranule is approximately $n_{funnel} = 34.2$. This value of n_{funnel} should also hold for equatorial regions of coronal holes that have super-radial solar-wind expansion.

On the photosphere the open flux funnels do not fill the area of the supergranule, but in the coronal-hole-origin solar wind in the heliosphere the funnels have expanded laterally to fill the volume; hence the area associated with a "supergranule" out in the heliosphere is filled with ~34 funnels. In the radially expanding solar wind, a supergranule with a diameter d_{super} on the photosphere has a diameter $D_{super} = r d_{super}$ a distance r out in the heliosphere. In the heliosphere the supergranule area D_{super}^2 must equal $34.2 D_{funnel}^2$, so $D_{funnel} = D_{super}/34.2^{1/2} = D_{super}/5.8$. Linearly, a supergranule has 5.8 funnels across it.

As an aside, at 1 AU where the radial magnetic-field strength is B_r the funnel diameter D_{funnel} should be given by flux conservation $D_{funnel}^2 B_r = d_{bp}^2 B_{bp}$; for $B_r = 2.3$ nT (the average of the 66 intervals in Table 1, see Table 4), $d_{bp} \sim 150$ km, and $B_{bp} \sim 1500$ G the flux-conservation expression yields $D_{funnel} \sim 1.2 \times 10^6$ km; this value 1.2×10^6 km is a factor of 2 bigger than the median flux-tube size measured at 1 AU by *Borovsky* [2008] (see also *Neugebauer and Giacalone* [2015]).

To estimate how many funnels would be sampled by a spacecraft trajectory through the solar-wind plasma, two-dimensional cellularization patterns (magnetic cells, soap froth, etc.) can be examined [e.g. *Aboav*, 1983; *Weaire and Hutzler*, 1999; *Durand*, 2010]. In Figure 23 one such cellularization is shown. In the figure the two-dimensional square doubly-periodic box contains 150 cells with the cells all of approximately the same area; for the cells representing funnels out in the heliosphere, with the numerical value of 34.2 funnels per supergranule, the box in Figure 23 is 2.1 supergranule diameters by 2.1 supergranule diameters in area. 26 vertical cuts were made through the box in Figure 23 and 26 horizontal cuts were made through the box and along each cut the number of different funnels that the cut line passed through was counted. The mean number of funnels encountered per cut was 14.2, where the cut lengths were all $12.2 = 150^{1/2}$ funnel diameters long. That is 1.16 funnel encounters per funnel diameter of pathway. For 5.8 funnel diameters per supergranule diameter a path will on average encounter 6.7 funnels per supergranule diameter of distance.

Note that the calculations in this section, and Figure 23, have taken the funnels to all have the same diameter (from the bright point bases all taken to have the same diameter and same magnetic-field strength). Certainly G-band bright points have a spectrum of diameters and field strength [*Ishikawa et al.*, 2007; *Utz et al.*, 2013; *Yang et al.*, 2014; *Criscuoli and Uitenbroek*, 2014], so the funnel sizes in the heliosphere will have a spectrum of diameters. The spectrum of diameters will alter the count-rate of funnel crossings.

One view of the source of solar-wind plasma in coronal holes is that at the Sun plasma is fed into the open-flux funnels by reconnection with newly emerged closed flux loops as the closed flux loops are advected into the supergranule-boundary lane where the open funnels reside [*Gabriel*, 1976; *Tu et al.*, 2005; *Wilhelm et al.*, 2011; *Yang et al.*, 2013]. The orientation, altitudes, field strengths, and Alfven speeds of the closed loops that reconnect with an open funnel will vary with time, so the reconnection rate between an open funnel and the closed loops will vary with time [e.g. *Fisk et al.*, 1999; *Axford et al.*, 1999; *He et al.*, 2010; *Yang et al.*, 2013]. There will also be variations in the reconnection rates from open funnel to open funnel. Hence one should expect the plasma supply to have variations from funnel to funnel, and even have variations within a funnel. Energy transfer to the open funnels by reconnection will also vary with time and with location within the funnel. From

these reconnection variations, a nonhomogenous solar-wind plasma coming out of the coronal-hole is a reasonable expectation. An inhomogeneity scale of funnel sizes is also a reasonable expectation.

7.2 Possible Effects from in situ Solar-Wind Turbulence

If turbulence is active in the coronal-hole-origin solar-wind plasma, the action of eddy diffusion is expected to blend away structure in the solar-wind plasma, producing an increase in the structure scalesizes with distance from the Sun.

To estimate the scale sizes that might be subject to eddy diffusion by MHD turbulence in the coronal-hole-origin solar wind the assumption will be made that fluctuations in the velocity (and magnetic field) in the coronal-hole-origin solar wind are active turbulence and that the transport of energy in the turbulence is at the eddy-turnover timescale. The scale sizes are estimated using the methodology of Sect. 5.1 of *Borovsky and Denton* [2010]. The scale $L_\perp$ perpendicular to the solar-wind magnetic field over which turbulent eddy diffusion could transport plasma is given by

$$L_\perp \sim (D_{\perp\perp} \tau_{age})^{1/2} \qquad , \qquad (4)$$

where $D_{\perp\perp}$ is the MHD eddy-diffusion coefficient and τ_{age} is the age of the solar-wind plasma from its birth at the Sun. At a distance r from the sun, the age of the plasma is the advection timescale $\tau_{age} = r/v_r$. The eddy-diffusion coefficient $D_{\perp\perp}$ is approximated by $D_{\perp\perp} \sim L_{eddy}^2/\tau_{eddy}$ where L_{eddy} is the large-eddy scale size in the turbulence and τ_{eddy} is the eddy-turnover timescale for a large eddy. That turnover time is $\tau_{eddy} \sim L_{eddy}/v_{rms}$, where v_{rms} is the velocity-fluctuation amplitude of the turbulence, which is $v_{rms} \sim v_A$. Thus $D_{\perp\perp} \sim L_{eddy} v_A$ for strong turbulence. The large-eddy scale size is usually taken to be the scale associated with the low-frequency breakpoint in the Fourier spectrum of magnetic-field fluctuations, which is $L_{eddy} = v_r \tau_{break}$ where $\tau_{break} = 1/f_{break}$ is the timescale associated with the breakpoint frequency f_{break} of the Fourier spectrum. Since we are interested in the large-eddy scalesize perpendicular to the mean magnetic field, a $\sin(\theta_{Ps})$ factor is put into the expression $L_{eddy} = v_r \tau_{break} \sin(\theta_{Ps})$ to account for the angle θ_{Ps} between the solar wind vector $\underline{v}$ and the direction of the Parker-spiral. Because of the wiggling of the solar-wind magnetic field about the Parker-spiral direction (which increases with distance from the Sun but decreases when averaged over the

timescale τ_{break} [*Borovsky*, 2010]), the $\sin(\theta_{Ps})$ factor will lead to an underestimate of L_{eddy}. Taking $D_{\perp\perp} \sim v_r \tau_{break} \sin(\theta_{Ps}) v_A$ and $\tau_{age} = r/v_r$, expression (4) becomes

$$L_\perp \sim (\tau_{break} \, v_A \, r \, \sin(\theta_{Ps}))^{1/2} \quad . \tag{5}$$

For an estimate of the breakpoint timescale τ_{break} in the coronal-hole solar wind, the expression $\tau_{break} = 1300$ s $R^{1.5}$ can be used, where $R = r/(1$ AU$)$ is the dimensionless distance from the Sun. The expression $\tau_{break} = 1300$ s $R^{1.5}$ comes from the f_{break} curve in Fig. 30 of *Bruno and Carbone* [2013] with $\tau_{break} = 1/f_{break}$. (Note that the values $\tau_{break} = 1300$ s $R^{1.5}$ are 2 to 4 times greater than values given for the coronal-hole solar wind in Fig. 3 of *Horbury et al.* [1996].)

At 1 AU with $\tau_{break} \sim 1300$s, $v_A = 67$ km/s (from the average of all solar-wind measurements in the 66 intervals of unperturbed coronal-hole plasma in Table 1), $\theta_{Ps} = 33°$ at $v_r = 632$ km/s (average from Table 4), and $r = 1$ AU $= 1.5 \times 10^8$ km, expression (5) gives $L_\perp \sim 2.6 \times 10^6$ km. For a heliospheric Parker-spiral pattern that rotates in the ecliptic plane at a speed of 400 km/s at 1 AU, the scale size $L_\perp = 2.6 \times 10^6$ km corresponds to a timescale $\Delta t = 6500$ s. With a solar-wind-origin footpoint moving at about 0.5 km/s on the photosphere (cf. Table 8), the timescale 6500 s yields $L_{sun} \sim 3200$ km for the scale size of solar-wind eddy diffusion on the spacecraft measurements scaled to photospheric distances. (Without the factor $\sin(\theta_{Ps})$, the estimate $L_{sun} \sim 4400$ km would be obtained.)

At 2.25 AU in the Ulysses polar crossings the expression $\tau_{break} = 1300$ s $R^{1.5}$ yields $\tau_{break} = 4400$ s; the average value of the Alfven speed v_A for Polar Crossings 1 and 2 is $v_A = 44$ km/s; and the average speed for Polar Crossings 1 and 2 is 778 km/s yielding $\theta_{Ps} = 9.5°$. With these values, expression (5) yields $L_\perp \sim 3.3 \times 10^6$ km. At a latitude of 80° and a distance of 2.25 AU, the rotation speed of the Parker-spiral pattern past the Ulysses spacecraft is 130 km/s, so the scale size $L_\perp \sim 3.3 \times 10^6$ km corresponds to a timescale $\Delta t = 2.5 \times 10^4$ s in the spacecraft measurements. With a solar-wind-origin footpoint moving at about 0.25 km/s on the photosphere (cf. Table 8), this timescale yields $L_{sun} \sim 6300$ km for the scale size of solar-wind eddy diffusion on the spacecraft measurements scaled to photospheric distances. (Without the factor $\sin(\theta_{Ps})$, the estimate $L_{sun} \sim 12000$ km would be obtained.)

At 0.3 AU the expression $\tau_{break} = 1300$ s $R^{1.5}$ yields $\tau_{break} = 210$ s; the average value of v_A for Helios Flattop Intervals 2 and 5 at 0.3 AU is $v_A = 161$ km/s; and with an average

velocity of 665 km/s for the Helios Flattop Intervals 2 and 5 the value $\theta_{Ps} = 10^o$ is obtained. With these values, expression (5) yields $L_\perp \sim 5.1 \times 10^5$ km. For the fast-moving Helios spacecraft, the speed of the spacecraft through the rotating Parker-spiral pattern is 90 km/s, so the scale size $L_\perp \sim 5.1 \times 10^5$ km corresponds to a timescale of $\Delta t = 5900$ s in the spacecraft measurements. With a solar-wind-origin footpoint moving at about 0.25 km/s on the photosphere (cf. Table 8), this timescale yields $L_{sun} \sim 1400$ km for the scale size of solar-wind eddy diffusion on the spacecraft measurements scaled to photospheric distances. (Without the factor $\sin(\theta_{Ps})$, the estimate $L_{sun} \sim 3400$ km would be obtained.)

The characteristic scale sizes (mapped to the photosphere) for the action of eddy diffusion in the coronal-hole solar wind are 1400 km to 3400 km for measurements at 0.3 AU, 3200 km to 4400 km for measurements at 1 AU, and 6300 km to 12000 km for measurements at 2.3 AU. If turbulence in the solar wind were acting at these estimated spatial scales (1) structure smaller than these scales would be greatly reduced and (2) there would be an evolution of the structure scales with distance from the Sun. At 0.3 AU and at 1 AU, the structure scalesizes seen in the spacecraft measurements are larger than these estimated turbulent-diffusion scalesizes. Certainly, at 2.3 AU structure finer than the 12000-km turbulent-diffusion scale is seen: see for example structure in the helium abundance ratio α/p in Figure 20 and structure in B_{mag}/n_p in Figure 17. At 2.3 AU the turbulence estimate of 6300 km could be effectively limiting the scalesizes of the observed structure in the coronal-hole-origin plasma. However, in general there is a lack of evolution of structure scale sizes with distance from the Sun, as exemplified by Figure 17; this might argue that the lower limit to the structure scales sizes at 2.3 AU is not caused by the action of turbulent diffusion in the solar wind.

7.3. Comparison of Expectations with Observations

Expectations for a coronal-hole solar wind born in open-flux magnetic funnels are that there should be about 6.7 funnel crossings per supergranule diameter for a spacecraft in the heliosphere mapped back to the solar surface. This is roughly the scalesize of plasma variation seen in the unperturbed coronal-hole solar wind when various parameters are measured and mapped to the solar surface. Hence, the plasma structure seen by spacecraft in

the coronal-hole-origin solar wind is consistent with relic structure from the birth of the solar wind.

Estimates of turbulent-diffusion scalesizes in the solar wind at 0.3 AU, 1 AU, and 2.3 AU yield diffusion scales smaller than the structure scalesizes seen in the coronal-hole-origin solar wind. Hence, except perhaps at 2.3 AU and further from the Sun, turbulent eddy diffusion is not affecting the structures observed in the coronal-hole-origin solar wind.

References

Aboav, D. A., The arrangements of cells in a net. II, *Metallography, 16*, 265, 1983.

Antonucci, E., L. Abbo, and M. A. Dodero, Slow wind and magnetic topology I the solar minimum corona in 1996-1997, *Astron. Astrophys., 435*, 699, 2005.

Arge, C.N., D. Odstrcil, V.J. Pizzo, and L.R. Mayer, Improved method for specifying solar wind speed near the sun. In: *The Tenth International Solar Wind Conference. AIP, Melville, NY*, pp.190–193, 2003.

Axford, W. I., J. F. McKenzie, G. V. Sukhorukova, M. Banaszkiewicz, A. Czechowski, and R. Ratkievicz, Acceleration of the high speed solar wind in coronal holes, *Space Sci. Rev., 87*, 25, 1999.

Balogh, A., T. J. Beek, R. J. Forsyth, P. C. Hedgecock, R. J. Marquedant, E. J. Smith, D. J. Southwood, and B. T. Tsurutani, The magnetic field investigation on the Ulysses mission: Instrumentation and preliminary scientific results, *Astron. Astrophys. Suppl. Ser., 92*, 221, 1992.

Balogh, A., R. J. Forsyth, . A. Lucek, T. S. Horbury, and E. J. Smith, *Geophys. Res. Lett., 26,* 631, 1999.

Bame, S. J., J. R. Asbridge, W. C. Feldman, and J. T. Gosling, Solar cycle evolution of high-speed solar wind streams, *Astrophys. J., 207*, 977, 1976.

Bame, S. J., J. R. Asbridge, W. C. Feldman, and J. T. Gosling, Evidence for a structure-free state at high solar wind speeds, *J. Geophys. Res., 82*, 1487, 1977.

Bame, S. J., D. J. McComas, B. L. Barraclough, J. L. Phillips, K. J. Sofaly, J. C. Chaves, B. E. Goldstein, and R. K. Sakurai, The Ulysses solar wind plasma experiment, *Astron. Astrophys. Suppl. Ser., 92*, 237, 1992.

Bavassano, B., and R. Bruno, On the role of interplanetary sources in the evolution of low-frequency Alfvenic turbulence in the solar wind, *J. Geophys. Res., 97*, 19129, 1992.

Bavassano, B., E. Pietropaolo, and R. Bruno, Compressive fluctuations in high-latitude solar wind, *Ann. Geophys., 22*, 689, 2004.

Belcher, J. W., and L. Davis, Large-amplitude Alfven waves in the interplanetary medium, 2, *J. Geophys. Res., 76,* 3534, 1971.

Borovsky, J. E., The flux-tube texture of the solar wind: Strands of the magnetic carpet at 1 AU, *J. Geophys. Res., 113,* A08110, 2008.

Borovsky, J. E., On the variations of the solar-wind magnetic field about the Parker-spiral direction, *J. Geophys.* Res., 115, A09101, 2010.

Borovsky, J. E., The effect of sudden wind shear on the Earth's magnetosphere: Statistics of wind-shear events and CCMC simulations of magnetotail disconnections, *J. Geophys. Res., 117,* A06224, 2012a.

Borovsky, J. E., Looking for evidence of mixing in the solar wind from 0.31 to 0.98 AU, *J. Geophys. Res., 117,* A06107, 2012b.

Borovsky, The velocity and magnetic-field fluctuations of the solar wind at 1 AU: Statistical analysis of Fourier spectra and correlations with plasma properties, *J. Geophys. Res., 117,* A05104, 2012c.

Borovsky, J. E., and M. H. Denton, Solar-wind turbulence and shear: A superposed-epoch analysis of corotating interaction regions at 1 AU, *J. Geophys. R*es., 115, A10101, 2010.

Borovsky, J. E., and M. H. Denton, The trailing edges of high-speed streams at 1 AU, submitted to *J. Geophys. Res.*, 2016JA022863, 2016.

Borovsky, J. E., and S. P. Gary, How important are the alpha-proton relative drift and the electron heat flux for the proton heating of the solar wind in the inner heliosphere?, *J. Geophys. Res., 119, 5210,* 2014.

Borovsky, J. E., and J. T. Steinberg, The freestream turbulence effect in solar-wind/magnetosphere coupling: Analysis through the solar cycle and for various types of solar wind, *Geophys. Monog. Ser., 167,* 59, 2006.

Borovsky, J. E., and J. T. Steinberg, No evidence for the localized heating of solar-wind protons at intense velocity shear zones, *J. Geophys. Res.,* 119, 1455, 2014.

Borrini, G., J. T. Gosling, S. J. Bame, W. C. Feldman, and J. M. Wilcox, Solar wind helium and hydrogen structure near the heliospheric current sheet: A signal of coronal streamers at 1 AU, *J. Geophys. Res., 86,* 4565, 1981.

Bruno, R., and V. Carbone, The solar wind as a turbulence laboratory, *Living Rev. Solar Phys. 10*, 2, http://www.livingreview.org/lrsp-2013-2, 2013.

Bruno, R., B. Bavassano, and U. Villante, Evidence for long period Alfven waves in the inner solar system, *J. Geophys. Res., 90*, 4373, 1985.

Burlaga, L. F., W. H. Mish, and Y. C. Whang, Coalescence of recurrent streams of different sizes and amplitudes, *J. Geophys. Res., 95,* 4247, 1990.

Carovillano, R. L., and G. L. Siscoe, Corotating structure in the solar wind, *Solar Phys., 8*, 401, 1969.

Cranmer, S. R., Coronal holes, *Living Rev. Solar Phys., 6*, 3, 2009.

Criscuoli, S., and H. Uitenbroek, The statistical distribution of the magnetic-field strength in G-band bright points, *Astron. Astrophys., 562*, L1, 2004.

Crooker, N. U., E. M. Appleton, N. A. Schwadron, and M. J. Owens, Suprathermal electron flux peaks at stream interfaces: Signature of solar wind dynamics or tracer for open magnetic flux transport on the Sun?, *J. Geophys. Res., 115*, A11101, 2010.

Culhane, J. L., D. H. Brooks, L. van Driel-Gesztelyi, P. Demoulin, D. Baker, M. L. DeRosa, C. H. Mandrini, L. Zhoa, and T. H. Zurbuchen, Tracking solar active region outflow plasma from its source to the near-Earth environment, *Solar Phys., 289,* 3799, 2014.

DeForest, C. E., J. T. Hoeksema, J. B. Gurman, B. J. Thompson, S. P. Plunkett, R. Howard, R. C. Harrison, and D. M. Hassler, Polar plume anatomy: Results of a coordinated observation, *Solar Phys., 175*, 393, 1997.

De Keyser, J., M. Roth, and A. Soding, Flow shear across solar wind discontinuities: WIND observations, *Geophys. Res. Lett., 25*, 2649, 1998.

Denskat, K. U., and F. M. Neubauer, Properties of low-frequency magnetic field fluctuations in the solar wind from 0.29 to 1.0 AU during solar minimum conditions: HELIOS 1 ad HELIOS 2, *J. Geophys. Res., 87,* 2215, 1982.

Dowdy, J. F., A. G. Emslie, and R. L. Moore, On the inability of magnetically constricted transition regions to account for the 10^5 to 10^5 K plasma in the quiet solar atmosphere, *Solar Phys., 112*, 255, 1987.

Du, D., B. Zuo, and X. X. Zhang, Interplanetary coronal mass ejections observed by Ulysses through its three solar orbits, *Solar Phys., 262*, 171, 2010.

Durand, Statistical mechanics of two-dimensional foams, *Eur. Phys. Lett., 90,* 60002, 2010.

Ebert, R. W., D. J. McComas, H. A. Elliot, R. J. Foster, and J. T. Gosling, Bulk properties of the slow and fast solar wind and interplanetary coronal mass ejections measured by Ulysses: Three polar orbits of observations, *J. Geophys. Res., 114,* A01109, 2009.

Elliott, H. A., D. J. McComas, N. A. Schwadron, J. T. Gosling, R. M. Skoug, G. Gloeckler, and T. H. Zurbuchen, An improved expected temperature formula for identifying ICMEs, *J. Geophys. Res., 110*, A04103, 2005.

Feldman, W. C. J. R. Asbridge, S. J. Bame, and J. T. Gosling, High-speed solar wind flow parameters at 1 AU, *J. Geophys. Res., 81*, 5054, 1976a.

Feldman, W. C., J. R. Asbridge, S. J. Bame, S. P. Gary, M. D. Montgomery, and S. M. Zink, Evidence for the regulation of solar wind heat flux at 1 AU, *J. Geophys. Res. 81*, 5207, 1976b.

Feldman, W. C., J. R. Asbridge, S. J. Bame, J. T. Gosling, and D. S. Lemons, Characteristic electron variations across simple high-speed solar wind streams, *J. Geophys. Res., 83*, 5285, 1978.

Fisher, R., and M. Guhathakurta, Physical properties of polar coronal rays and holes as observed with the Spartan 201-01 coronograph, *Astrophys. J., 447*, L139, 1995.

Fisk, L. A., T. H. Zurbuchen, and N. A. Schwadron, On the coronal magnetic field: Consequences of large-scale motions, *Astrophys. J., 521*, 868, 1999.

Fitzenreiter, R. J., K. W. Ogilvie, D. J. Chornay, and J. Keller, Observations of electron velocity distribution functions in the solar wind by the WIND spacecraft: High angular resolution strahl measurements, *Geophys. Res. Lett., 25*, 249, 1998.

Freeman, J. W., and R. E. Lopez, The cold solar wind, *J. Geophys. Res., 90*, 9885, 1985.

Gabriel, A. H., A magnetic model of the solar transition region, *Phil. Trans. R. Soc. Lond. A., 281*, 339, 1976.

Gloeckler, G., J. Cain, F. M. Ipavich, E. O. Tums, P. Bedini, L. A. Fisk, T. H. Zurbuchen, p. Bachsler, J. Fischer, R. F. Wimmer-Schweingruber, J. Geiss, and R. Kallenbach, Investigation of the composition of solar and interstellar matter using solar wind and pickup ion measurements with SWICS and SWIMS on the ACE spacecraft, *Space Sci. Rev., 86*, 497, 1998.

Gloeckler, G., T. H. Zurbuchen, and J. Geiss, Implications of the observed anticorrelation between solar wind speed and coronal electron temperature, *J. Geophys. Res., 108*, 1158, 2003.

Gosling, J. T., V. Pizzo, and S. J. Bame, Anomalously low proton temperatures in the solar wind following interplanetary shock waves -- Evidence for magnetic bottles, *J. Geophys. Res., 78*, 2001, 1973.

Gosling, J. T., G. Borrini, J. R. Asbridge, S. J. Bame, W. C. Feldman, and R. T. Hansen, Coronal streamers in the solar wind at 1 AU, *J. Geophys. Res., 86*, 5438, 1981.

Gosling, J. T., D. N. Baker, S. J. Bame, W. C. Feldman, R. D. Zwickl, and E. J. Smith, Bidirectional solar wind electron heat flux events, *J. Geophys. Res., 92*, 8519, 1987.

Gosling, J. T., C. A. de Koning, R. M. Skoug, J. T. Steinberg, and D. J. McComas, Dispersionless modulation in low-energy solar electron bursts and discontinuous changes in the solar wind electron strahl, *J. Geophys. Res., 109,* A05102, 2004.

Gosling, J. T., D. J. McComas, D. A. Roberts, and R. M. Skoug, A one-sided aspect of Alfvenic fluctuations in the solar wind, *Astrophys. J., 695*, L213, 2009.

Gosling, J. T., H. Tian, and T. D. Phan, Pulsed Alfven waves in the solar wind, *Astrophys. J., 737*, L35, 2011.

Hagenaar, H. J., C. J. Schriver, and A. M. Title, The distribution of cell sizes of the solar chromosphere network, *Astrophys. J., 481*, 998, 1997.

Hammond, C. M., W. C. Feldman, D. J. McComas, J. L. Phillips, and R. J. Forsyth, Variation of electron-strahl width in the high-speed solar wind: Ulysses observations, *Aston. Astrophys., 316*, 350, 1996.

He, J.-S., C.-Y. Tu, H. Tian, and E. Marsch, Solar wind origins in coronal holes and in the quiet Sun, *Adv. Space Res., 45*, 303, 2010.

Hellinger, P., L. Matteini, S., Stverak, P. M. Travnicek, and E. Marsch, Heating and cooling of protons in the fast solar wind between 0.3 and 1 AU: Helios revisited, *J. Geophys. Res., 116*, A09105, 2011.

Horbury, T. S., a. Balogh, R. J. Forsyth, and E. J. Smith, The rate of evolution over the Sun's poles, *Astron. Astrophys., 316*, 333, 1996.

Ishikawa, R., S. Tsuneta, Y. Katakosi, Y. Katsukawa, J. A. Bonet, S. Vargas Dominguez, L. H. M. Rouppe van der Voort, Y. Sakamoto, and T. Ebisuzaki, Relationships between magnetic foot points and G-band bright structures, *Astron. Astrophys., 472*, 911, 2007.

Kahler, S. W., N. U. Crooker, and J. T. Gosling, The topology of intrasector reversals of the interplanetary magnetic field, *J. Geophys. Res., 101*, 24373, 1996.

Kasper, J. C., A. J. Lazarus, J. T. Steinberg, K. W. Ogilvie, and A. Szabo, Physics-based tests to identify the accuracy of solar wind ion measurements: A case study with the Wind Faraday Cups, *J. Geophys. Res., 111*, A03105, 2006.

Kayshap, P., D. Banerjee, and A. K. Srivastava, Diagnostics of a coronal hole and the adjacent quiet Sun by the Hinode/EUV Imaging Spectrometer (EIS), *Solar Phys., 290*, 2889, 2015.

King, J. H., and N. E. Papitashvili, Solar wind spatial scales in and comparisons of hourly Wind and ACE plasma and magnetic field data, *J. Geophys. Res., 110*, 2104, 2005.

Ko, Y.-K., K. Muglach, Y.-M. Wang, P. R. Young, and S. T. Lepri, Temporal evolution of solar wind ion composition and their source coronal holes during the declining phase of Cycle 23. I. Low-latitude extension of polar coronal holes, Astrophys. J., 787, 121, 2014.

Kojima, M., K. Fujiki, T. Ohmi, M. Tokumaru, A. Yokobe, and K. Hakamada, Low-speed solar wind from the vicinity of solar active regions, J. Geophys. Res., 104, 16993, 1999.

Krieger, A. S., A. F. Timothy, and E. C. Roelof, A coronal hole and its identification as the source of a high velocity solar wind stream, *Solar Phys., 29*, 505, 1973.

Landi, E., R. L. Alexander, J. R. Gruesbeck, J. A. Gilbert, S. T. Lepri, W. B. Manchester, and T. H. Zurbuchen, Carbon ionization stages as a diagnostic of the solar wind, *Astrophys. J., 744*, 100, 2012.

Leamon, R. J., and S. W. McIntosh, How the solar wind ties to its photospheric origins, *Astrophys. J., 697*, L28, 2009.

Lepping, R. P., M. H. Acuna, L. F. Burlaga, W. M. Farrell, J. A. Slavin, K. H. Schatten, F. Mariani, N. F. Ness, F. M. Neubauer, Y. C. Whang, J. B. Byrnes, R. S. Kennon, P. V. Panetta, J. Scheifele, and E. M. Worley, The WIND Magnetic Field Investigation, *Space Sci. Rev., 71*, 207, 1995.

Lepping, R. P., C.-C. Wu, and D. B. Berdichevsky, Automatic identification of magnetic cloud-like regions at 1 AU: occurrence rate and other properties, *Ann. Geophys., 23*, 2687, 2005.

Levine, R. H., M. D. Altschuler, and J. W. Harvey, Solar sources of the interplanetary magnetic field and solar wind, *J. Geophys. Res., 82*, 1061, 1977.

Lin, R. P., K. A. Anderson, S. Ashford, C. Carlson, D. Curtis, R. Ergun, D. Larson, J. McFadden, M. McCarthy, G. K. Parks, H. Reme, J. M. Bosqued, J. Coutelier, F. Cotin, C. D'uston, K.-P. Wenzel, T. R. Sanderson, J. Henrion, J. C. Ronnet, and G. Paschmann, A three-dimensional plasma and energetic particle investigation for the WIND spacecraft, *Space Sci. Rev., 71*, 125, 1995.

Lopez, R. E., Solar cycle invariance in solar wind proton temperature relationships, J. Geophys. Res., 92, 11189, 1987.

Louarn, P., C. Dieval, V. Genot, B. Lavraud, A. Opitz, A. Fedorov, J. A. Sauvaud, D. Larson, A. Galvin, M. H. Acuna, and J. Luhmann, On the temporal variability of the "strahl" and

its relationship with solar wind characteristics: STEREO SWEA observations, *Solar Phys., 259*, 311, 2009.

Marsch, E., K.-H. Muhlhauser, H. Rosenbauer, R. Schwenn, and F. M. Neubauear, Solar wind helium ions: Observations of the Helios solar probes between 0.3 and 1 AU, *J. Geophys. Res., 87*, 35, 1982.

McComas, D. J., B. L. Barraclough, J. T. Gosling, C. M. Hammond, J. L. Phillips, M. Neugebauer, A. Balogh, and R. J. Forsyth, Structures in the polar solar wind: plasma and field observations from Ulysses, *J. Geophys. Res., 100*, 19893, 1995.

McComas, D. J., S. J. Blame, P. Barker, W. C. Feldman, J. L. Phillips, P. Riley, and J. W. Griffee, Solar Wind Electron Proton Alpha Monitor (SWEPAM) for the Advanced Composition Explorer, *Space Sci. Rev. 86*, 563, 1998.

McComas, D. J., H. A. Elliott, J. T. Gosling, D. B. Reisenfeld, R. M. Skoug, B. E. Goldstein, M. Neugebauer, and A. Balogh, Ulysses' second fast-latitude scan: Complexity near solar maximum and reformation of polar coronal holes, *Geophys. Res. Lett., 29*, 1920, 2002.

Neugebauer, M., Alignment of velocity and field changes across tangential discontinuities in the solar wind, *J. Geophys. Res., 90*, 6627, 1985.

Neugebauer, M., Comment on the abundances of rotational and tangential discontinuities in the solar wind, *J. Geophys. Res., 111*, A04103, 2006.

Neugebauer, M., Evidence for polar x-ray jets as sources of microstream peaks in the solar wind, *Astrophys. J., 750,* 50, 2012.

Neugebauer, M., and J. Giacalone, Energetic particles, tangential discontinuities, and solar flux tubes, *J. Geophys. Res., 120*, 8281, 2015.

Neugebauer, M., and B. E. Goldstein, Double-proton beams and magnetic switchbacks in the solar wind, *AIP Conf. Proc., 1539*, 46, 2013.

Neugebauer, M., B. E. Goldstein, D. J. McComas, S. T. Suess, and A. Balogh, Ulysses observations of microstreams in the solar wind from coronal holes, *J. Geophys. Res., 100*, 23389, 1995.

Neugebauer, M., B. E. Goldstein, E. J. Smith, and W. C. Feldman, Ulysses observations of differential alpha-proton streaming in the solar wind, *J. Geophys. Res., 101*, 17047, 1996.

Neugebauer, M., A. Ruzmaikin, and D. J. McComas, Wavelet analysis of the structure of microstreams in the polar solar wind, *AIP Conf. Proc., 385,* 41, 1997.

Neugebauer, M., B. E. Goldstein, D. Winterhalter, E. J. Smith, R. J. MacDowall, and S. P. Gary, Ion distributions in large magnetic holes in the fast wind, *J. Geophys. Res., 106*, 5635, 2001.

Neugebauer, M., J. T. Steinberg, R. L. Tokar, B. L. Barraclough, E. E. Dors, R. C. Weins, D. E. Gingerich, D. Luckey, and D. B. Whiteaker, Genesis on-board determination of the solar wind flow regime, *Space Sci. Rev., 105*, 661, 2003.

Neugebauer, M., G. Gloeckler, J. T. Gosling, A. Rees, R. Skoug, B. E. Goldstein, T. P. Armstrong, M. R. Combi, T. Makinen, D. J. McComas, R. von Steiger, T. H. Zurbuchen, E. J. Smith, J. Geiss, and L. J. Lanzerotti, Encounter of the Ulysses spacecraft with the ion tail of comet McNaught, *Astrophys. J., 667*, 1262, 2007.

Nodes, T. A., and N. C. Gallagher, Median filters: Some modifications and their properties, *IEEE Trans. Acoustic. Speech Signal Proc., 30*, 739, 1982.

Ogilvie, K. W., et al., SWE, a comprehensive plasma instrument for the WIND spacecraft, *Space Sci. Rev., 71*, 55, 1995.

Pagel, A. C., N. U. Crooker, T. H. Zurbuchen, and J. T. Gosling, Correlation of solar wind entropy and oxygen ion charge state ratio, *J. Geophys. Res., 109*, A01113, 2004.

Parhi, S., S. T. Suess, and M. Sulkanen, The generation of smooth high speed solar wind from plume-interplume mixing, *AIP Conf. Proc., 471*, 433, 1999.

Peter, H., Modeling the (upper) solar atmosphere including the magnetic field, *Adv. Space Res., 39*, 1814, 2007.

Podesta, J. J., Evidence of kinetic Alfven waves in the solar wind at 1 AU, *Solar Phys., 286*, 529, 2013.

Poletto, G., Sources of solar wind over the solar activity cycle, *J. Adv. Res., 4,* 215, 2013.

Reisenfeld, D. B., D. J. McComas, and J. T. Steinberg, Evidence of a solar origin for pressure balance structures in the high-latitude solar wind, *Geophys. Res. Lett., 26*, 1805, 1999.

Reisenfeld, D. B., J. T. Gosling, R. J. Forsyth, P. Riley, and O. C. St. Cyr, Properties of high-latitude CME-driven disturbances during Ulysses second northern polar passage, *Geophys. Res. Lett., 30*, 8031, 2003.

Reisenfeld, D. B., R. C. Weins, B. L. Barraclough, J. T. Steinberg, M. Neugebauer, J. Raines, and T. H. Zurbuchen, Solar wind conditions and composition during the Genesis mission as measured by in situ spacecraft, *Space Sci. Rev., 175,* 125, 2013.

Richardson, I. G., The formation of CIRs at stream-stream interfaces and resultant geomagnetic activity, in *Recurrent Magnetic Storms*, B. Tsurutani, R. McPherron, W. Gonzalez, G. Lu, J. H. A. Sobral, and N. Goalswamy (eds.), pg. 45, American Geophysical Union, 2006.

Richardson, I. G., Identification of interplanetary coronal mass ejections at Ulysses using multiple solar wind signatures, *Solar Phys., 289*, 3843, 2014.

Richardson, I. G., and H. V. Cane, Near-Earth interplanetary coronal mass ejections during solar cycle 23 (1996-2009): Catalog and summary of properties, *Solar Phys., 264*, 189, 2010.

Richardson, I. G., E. W. Cliver, and H. V. Cane, Sources of geomagnetic activity over the solar cycle: Relative importance of coronal mass ejections, high-speed streams, and slow solar wind, *J. Geophys. Res., 105,* 18203, 2000.

Roberts, D. A., M. L. Goldstein, L. W. Klein, and W. H. Matthaeus, Origin and evolution of fluctuations in the solar wind: Helios observations and Helios-Voyager comparisons, *J. Geophys. Res., 92,* 12023, 1987.

Rosenbauer, H., R. Schwenn, E. Marsch, B. Meyer, H. Miggenrieder, M. D. Montgomery, K. H. Muhlhauser, W. Pilipp, W. Voges, and S. M. Zink, A survey on initial results of the Helios plasma experiment, *J. Geophys. Res., 42*, 561, 1977.

Safrankova, J., Z. Nemecek, P. Cagas, L. Prech, J. Pavlu, G. N. Zastenker, M. O. Riazantseva, and I. V. Koloskova, Short-scale variations of the solar wind helium abundance, *Astrophys. J.*, 778, 25, 2013.

Schwartz, S. J., W. C. Feldman, and S. P. Gary, The source of proton anisotropy in the high-speed solar wind, *J. Geophys. Res., 86,* 541, 1981.

Schwenn, Solar wind sources and their variations over the solar cycle, *Space Sci. Rev., 124*, 51, 2006.

Schwenn, R., K.-H. Muhlhauser, E. Marsch, and H. Rosenbauer, Two states of the solar wind at the time of solar activity minimum II. Radial gradients of plasma parameters in fast and slow streams, in *Solar Wind Four*, MPAE-W-100-81-31, pg. 126, Max Planck Institut fur Aeronomie, Lindau, Germany, 1981.

Scime, E. E., S. J. Bame, W. C. Feldman, S. P. Gary, and J. L. Phillips, Regulation of the solar wind electron heat flux from 1 to 5 AU: Ulysses observations, *J. Geophys. Res., 99*, 23401, 1994.

Simon, G. W., and R. B. Leighton, Velocity fields in the solar atmosphere. III. Large-scale motion, the chromospheric network, and magnetic fields, *Astrophys. J., 140*, 1120, 1964.

Siscoe, G., and D. Intriligator, Three views of two giant streams: Aligned observations at 1 AU, 4.6 AU, and 5.9 AU, *Geophys. Res. Lett., 20*, 2267, 1993.

Siscoe, G. L., L. Davis, P. J. Coleman, E. J. Smith, and D. E. Jones, Power spectra and discontinuities of the interplanetary magnetic field: Mariner 4, *J. Geophys. Res., 73*, 61, 1968.

Siscoe, G. L., B. Goldstein, and A. J. Lazarus, An East-West asymmetry in the solar wind velocity, *J. Geophys. Res., 74*, 1759, 1969.

Slemzin, V., L. Harra, A. Urnov, S. Kuzin, F. Goryaev, and D. Berghmans, Signatures of slow solar wind streams from active regions in the inner corona, Solar Phys., 286, 157, 2013.

Smith, C. W., M. H. Acuna, L. F. Burlaga, J. L'Heureux, N. F. Ness, and J. Scheifele, The ACE Magnetic Fields Experiment, *Space Sci. Rev., 86*, 611, 1998.

Smith, E. J., Solar cycle evolution of the heliospheric magnetic field: The Ulysses legacy, *J. Atmos. Solar-Terr. Phys., 73*, 277, 2011.

Srikanth, R., J. Singh, and K. P. Raju, Distribution of supergranule sizes, *Astrophys. J., 534,* 1008, 2000.

Susino, R., R. Ventura, D. Spadaro, A. Vourlidas, and E. Landi, Physical parameters along the boundaries of a mid-latitude streamer and its adjacent regions, *Astron. Astrophys., 488, 303*, 2008.

Suzuki, T. K., Forecasting solar wind speeds, *Astrophys. J., 640*, L75, 2006.

Thieme, K. M., E. Marsch, and R. Schwenn, Relationship between structures in the solar wind and their source regions in the corona, in *Proceedings of the Sixth International Solar Wind Conference, Vol. I*, V. J. Pizzo, T. Holzer, and D. G. Sime (eds.) pg. 317, Technical Note NCAR/TN-306+Proc, National Center for Atmospheric Research, Boulder, 1988.

Thieme, K. M., R. Schwenn, and E. Marsch, Are structures in high-speed streams signatures of coronal fine structures?, *Adv. Space Res., 9*(4), 127, 1989.

Thieme, K. M., E. Marsch, and R. Schwenn, Spatial structures in high-speed streams as signatures of fine structures in coronal holes, *Ann. Geophys., 8,* 713, 1990.

Timothy, A. F., A. S. Krieger, and G. S. Vaiana, The structure and evolution of coronal holes, *Solar Phys., 42*, 135, 1975.

Tu, C.-Y., C. Zhou, E. Marsch, L.-D. Xia, L. Zhao, J.-X. Wang, and k. Wilhelm, Solar wind origin in coronal funnels, *Science, 308*, 519, 2005.

Turner, J. M., L. F. Burlaga, N. F. Ness, and J. F. Lemaire, Magnetic holes in the solar wind, *J. Geophys. Res., 82,* 1921, 1977.

Utz, D., A. Hanslmeier, A. Veronig, O. Kuhner, R. Muller, J. Jurcak, and B. Lemmerer, Variations of magnetic bright point properties with longitude and latitude as observed by Hinode/SOT G-band data, *Solar Phys., 284*, 363, 2013.

van Driel-Gesztelyi, J. L. Culhane, D. Baker, P. Demoulin, c. H. Mandrini, M. L. DeRosa, A. P. Rouillard, A. Opitz, G. Stenborg, A. Vourlidas, and D. H. Brooks, Magnetic topology of active regions and coronal holes: Implications for coronal outflows and the solar wind, *Solar Phys., 281*, 237, 2012.

Vasquez, B. J., V. I. Abramenko, D. K. Haggerty, and C. W. Smith, Numerous small magnetic field discontinuities of Bartels rotation 2286 and the potential role of Alfvenic turbulence, *J. Geophys. Res., 112,* A11102, 2007.

von Steiger, R., T. H. Zurbuchen, and D. J. McComas, Oxygen flux in the solar wind: Ulysses observations, *Geophys. Res. Lett., 37*, L22101, 2010.

Wang, Y.-M., and N. R. Sheeley, Solar wind speed and coronal flux-tube expansion, *Astrophys. J.*, 355, 726, 1990.

Weaire, D., and S. Hutzler, *The Physics of Foams*, Oxford University Press, Oxford, 1999.

Wilhelm, K., L. Abbo, F. Auchere, N. Barbey, L. Feng, A. H. Gabriel, S. Giordano, S. Imada, A. Llebaria, W. H. Matthaeus, G. Poletto, N.-E. Raouafi, S. T. Suess, L. Teriaca, and Y.-M. Wang, Morphology, dynamics and plasma parameters of plumes and inter-plume regions in solar coronal holes, *Astron. Atrophys. Rev., 19*, 35, 2011.

Winterhalter, D., E. J. Smith, M. Neugebauer, B. E. Goldstein, and B. T. Tsurutani, The latitude distribution of solar wind magnetic holes, *Geophys. Res. Lett., 27*, 1615, 2000.

Woo, R., Detection of low-latitude plumes in the outer corona by Ulysses radio ranging measurements, *Astrophys. J., 464*, L95, 1996.

Woo, R., Ultra-fine-scale filamentary structures in the outer corona and the solar magnetic field, *Astrophys. J., 639*, L95, 2006.

Woo, R., and S. R. Habbal, Extension of coronal structure into interplanetary space, *Geophys. Res. Lett., 24*, 1159, 1997.

Xu, F., and J. E. Borovsky, A new 4-plasma categorization scheme for the solar wind, *J. Geophys. Res.*, *120*, 70, 2015.

Yang, L., J. He, H. Peter, C. Tu, W. Chen, L. Zhang, E. Marsch, L. Wang, X. Feng, and L. Yan, Injection of plasma into the nascent solar wind via reconnection driven by supergranular advection, *Astrophys. J., 770,* 6, 2013.

Yang, Y.-F., J.-B. Lin, S. Feng, K.-F. Ji, H. Deng, and F. Wang, Evolution of isolated G-band bright points: size, intensity and velocity, *Res. Astron. Astrophys., 14*, 741, 2014.

Xystouris, G., E. Sigala, and H. Mavromichalaki, A complete catalog of high-speed solar wind streams during Solar Cycle 23, *Solar Phys., 289*, 995, 2014.

Yamauchi, Y., S. T. Suess, and T. Sakurai, Relation between pressure balance structures and polar plumes from Ulysses high latitude observations, *Geophys. Res. Lett., 29,* 1383, 2002.

Yamauchi, Y., S. T. Suess, and T. Sakurai, Relation between polar plumes and fine structure in the solar wind from Ulysses high-latitude observations, *AIP Conf. Proc., 679,* 255, 2003.

Yamauchi, Y., S. T. Suess, J. T. Steinberg, and T. Sakurai, Differential velocity between solar wind protons and alpha particles in pressure balanced structures, *J. Geophys. Res., 109*, A03104, 2004.

Zastenker, G. N., I. V. Koloskova, M. O. Riazantseva, A. S. Yurasov, J. Safrankova, Z. Nemecek, L. Prech, and P. Cagas, Observation of fast variations of the helium-ion abundance in the solar wind, *Cosmic Res., 52*, 25, 2014.

Zhao, L., T. H. Zurbuchen, and L. A. Fisk, Global distribution of the solar wind during solar cycle 23: ACE observations, *Geophys. Res. Lett., 36*, L14104, 2009.

Zurbuchen, T. H., L. A. Fisk, G. Gloeckler, and R. von Steiger, The solar wind composition throughout the solar cycle: A continuum of dynamic states, *Geophys. Res. Lett., 29,* 1352, 2002.

Table 1. The collection of 66 intervals of unperturbed coronal-hole plasma at 1 AU. These are high-speed streams with "flattop" velocity profiles that were each inspected to ensure that they were unperturbed coronal-hole plasma. UCHP is an abbreviation for "unperturbed coronal-hole plasma". Missing times in the table indicate features that could not clearly be located.

Flat-top #	Year	Start UCHP Day	UT	End UCHP Day	UT	Prior SI Day	UT	Subsequent SI Day	UT	W_{flat} [hr]	W_{hss} [hr]	$<v_r>$ [km/s]	$<r^2 B_r>$ [nT AU]
1	2003	153	22	155	16	152	18			43		791±26	-3.44
2	2003	160	19	162	14					44		690±21	-2.93
3	2003	178	16	181	15	177	13	182	16	72	123	730±38	-4.08
4	2003	185	14	186	18	184	13			29		750±21	-2.68
5	2003	210	1	213	13	209	11	215	20	85	153	775±33	-4.16
6	2003	234	12	236	0	233	2	239	22	37	164	743±21	-3.44
7	2003	253	18	255	22	252	8	256	17	53	105	615±29	2.80
8	2003	344	18	349	5	342	10	351	12	108	218	765±37	-3.70
9	2004	43	16	46	16	43	1	48	4	73	123	656±34	3.46
10	2004	60	12	64	11	59	0	64	18	96	138	640±31	-2.67
11	2004	141	21	146	9	141	4	146	21	109	136	493±21	-2.79
12	2005	39	10	41	13	38	14	43	11	52	117	711±18	3.94
13	2005	65	21	69	3	65	7	71	10	79	147	687±38	3.18
14	2005	281	10	284	5	281	2	285	3	68	96	641±29	2.17
15	2005	308	13	311	12	306	19	312	10	72	135	661±29	2.51
16	2005	334	19	338	15	334	0	340	6	93	150	691±30	2.30
17	2005	362	2	364	1	361	14	365	9	48	90	686±21	2.78
18	2006	132	1	134	0	131	2	135	8	48	102	613±22	2.16
19	2006	158	11	161	0	157	16	162	12	62	115	630±25	2.06

20	2006	166	22	169	16	165	20	171	7	67	131	575±18	-2.64
21	2006	186	12	187	22	185	19	189	17	35	93	598±18	1.45
22	2006	213	19	215	17	212	10	216	12	47	97	549±14	1.22
23	2006	240	20	242	6	239	15	242	15	35	72	542±13	0.73
24	2006	294	4	297	0	293	19	298	23	69	124	569±37	2.16
25	2006	328	11	330	17	327	13	333	14	55	145	605±21	-2.51
26	2007	3	11	5	19	1	21	6	20	57	119	645±23	-2.24
27	2007	16	23	20	2	15	11	22	0	76	157	648±21	-2.11
28	2007	29	23	31	8	29	9	33	4	34	91	675±24	-2.61
29	2007	72	6	75	16	71	7	78	16	83	177	647±31	-1.81
30	2007	118	12	120	11	117	16	122	16	48	120	640±27	2.10
31	2007	128	14	129	11	127	14	130	1	22	59	601±13	-1.63
32	2007	139	7	140	6	138	11	141	4	24	65	616±18	-2.19
33	2007	145	4	148	3	144	1	148	17	72	111	653±23	2.50
34	2007	210	21	214	6	210	12	216	3	82	135	571±33	2.15
35	2007	239	9	240	17	238	18	242	17	33	94	638±17	1.52
36	2007	245	17	247	0					32		626±21	-2.10
37	2007	265	10	267	15	264	8	269	20	54	132	645±24	2.12
38	2007	292	15	293	15	291	18	294	15	25	69	640±19	2.68
39	2008	6	7	8	12	5	7	10	13	54	126	647±27	2.39
40	2008	15	1	20	1	13	13	22	9	121	212	642±29	-2.06
41	2008	33	0	35	5	32	8	37	8	54	120	600±15	3.11
42	2008	42	13	47	6	41	8	49	3	114	187	649±22	-2.01
43	2008	70	16	75	18	69	4	77	21	123	209	637±36	-2.01
44	2008	108	10	110	23	107	11	112	10	62	118	523±16	-1.59
45	2008	152	1	154	6	150	20	156	0	54	124	583±21	-2.34
46	2008	179	0	180	1	177	17	181	10	26	89	624±19	-1.67
47	2008	194	17	197	14	194	2	200	5	70	147	657±25	1.84
48	2008	205	4	206	3	204	13	206	16	24	51	631±11	-1.85
49	2008	223	5	224	16	222	11	227	0	36	109	624±13	1.65
50	2008	286	2	287	5	285	11	288	18	28	78	526±12	-1.91
51	2008	303	17	305	4	302	20	307	0	36	99	675±12	2.28
52	2009	232	22	235	0	232	1	235	8	51	78	510±19	1.05
53	2009	325	18	326	19	325	6	327	0	26	42	522±16	1.34
54	2010	168	0	169	13	166	14	170	5	38	87	527±13	-2.41
55	2010	181	10	185	8	180	18	187	21	95	171	610±26	1.43
56	2010	237	6	240	1	236	3	241	6	68	123	658±15	1.38
57	2010	297	5	299	11	295	19	301	13	55	138	628±23	1.48

58	2011	7	17	10	8	7	9	10	23	64	85	599±24	1.89
59	2011	93	5	94	12	92	5	95	0	32	66	578±19	1.29
60	2011	120	17	122	18	119	22	124	20	50	118	646±32	2.35
61	2011	174	16	176	11	173	19	178	22	44	123	606±13	2.15
62	2011	201	14	203	14	200	7	204	20	49	108	662±29	2.33
63	2012	104	10	105	16	103	15	106	8	31	65	580±22	1.69
64	2012	130	23	133	14	130	11	134	9	64	94	585±29	2.00
65	2012	157	12	158	23	156	5	162	3	36	142	690±24	2.31
66	2012	183	6	185	0	182	9	185	18	43	81	646±13	2.17

Table 2. The collection of five intervals of unperturbed coronal-hole plasma in the Helios 1 and Helios 2 data sets. Flattop Intervals 3 and 4 have poor data coverage.

Flattop Interval	Spacecraft	Year	Start UCHP		End UCHP		Distance [AU]	$\langle v_r \rangle$ [km/s]	$\langle r^2 B_r \rangle$ [nT AU]
			Day	UT	Day	UT			
1	Helios 1	1975	40	8	45	21	0.61-0.67	694±44	-3.10
2	Helios 1	1975	72	16	75	2	0.31	621±48	-3.01
3	Helios 1	1976	66		70		~0.5		
4	Helios 1	1976	75		79		~0.4		
5	Helios 2	1976	105	14	113	1	0.29-0.31	709±55	+2.76

Table 3. The collection of polar crossings by Ulysses (latitude >75°). The comet-McNaught encounter (Days 35-41 of 2007) was eliminated from Polar Crossing 5, splitting that crossing into the two intervals 5A and 5B. Polar Crossings 3 and 4 are not unperturbed coronal-hole plasma. Crossing 6 has limited data resolution.

Polar Crossing	Pole Crossed	Start		End		r [AU]	$\langle v_r \rangle$ [km/s]	$\langle r^2 B_r \rangle$ [nT AU]
		Year	Day	Year	Day			
1	south	1994	209	1994	293	2.0-2.6	769±23	-3.09
2	north	1995	184	1995	248	1.8-2.3	787±21	2.79
3	south	2000	282	2000	366	2.0-2.6	389±62	-0.67
4	north	2001	256	2001	320	1.8-2.3	732±41	-3.09
5A	south	2006	356	2007	34	2.4-2.7	769±19	2.40
5B	south	2007	42	2007	76	2.1-2.4	747±18	2.36
6	north	2007	350	2008	50	1.9-2.3	763±25	-1.97

Table 4. Mean values of various parameters of the 66 intervals of unperturbed coronal-hole plasma at 1 AU.

Quantity	Mean Value
W_{flat} width of flattop interval	57.1 hr
W_{hss} width of coronal hole	118 hr
v_r	632 km/s
n_p	2.4 cm^{-3}
B_{mag}	4.7 nT
$|B_r|$	2.27 nT
T_p	15.9 eV
α/p	3.8 %
B_{mag}/n_p	2.0 nT cm^3
v_A	67 km/s
$\log_{10}(S_p)$	0.92 [eV cm^2]

$\log_{10}(C^{6+}/C^{4+})$	-0.58
$\log_{10}(C^{6+}/C^{5+})$	-0.77
$\log_{10}(O^{7+}/O^{6+})$	-1.76
$\log_{10}(Fe/O)$	-1.02

Table 5. Correlation coefficients R_{corr} [in per cent] between the various averaged quantities for the 66 intervals of unperturbed coronal-hole plasma at 1 AU. With the 66 values, correlation at the 2σ level requires $|R_{corr}| > 24\%$.

	W_{hss}	$<v_r>$	$|<B_r>|$	$<B_{mag}>$	$<T_p>$	$<n_p>$	$<\alpha/p>$	$<\log(C^{6+}/C^{4+})>$	$<\log(O^{7+}/O^{6+})>$	$<\log(Fe/O)>$
W_{hss}	100	45	34	35	38	-5	-13	2	-3	-26
$<v_r>$	45	100	66	62	83	-7	17	-4	-5	-38
$|<B_r>|$	34	66	100	87	71	25	0	24	21	-34
$<B_{mag}>$	35	62	87	100	75	36	-8	45	39	-13
$<T_p>$	38	83	71	75	100	-10	-19	24	19	-16
$<n_p>$	-5	-7	25	36	-10	100	27	-10	-11	-33
$<\alpha/p>$	-13	17	0	-8	-19	27	100	-26	-15	-39
$<\log(C^{6+}/C^{4+})>$	2	-4	24	45	24	-10	-26	100	95	42
$<\log(O^{7+}/O^{6+})>$	-3	-5	21	39	19	-11	-15	95	100	45
$<\log(Fe/O)>$	-26	-38	-34	-13	-16	-33	-39	42	45	100

Table 6. Pearson linear correlation coefficients between hourly averaged values of several quantities in the 66 flattops at 1 AU. For each quantity there are between 3304 and 3769 hours of data available in the 66 intervals. The quantities v_r, S_p, v_A, n_p, T_p, B_{mag}, and α/p are from the OMNI2 data set; the quantities O^{7+}/O^{6+}, C^{6+}/C^{5+}, and C^{6+}/C^{4+}, and Fe/O are from the ACE SWICS 1p1 data set; f_{272} is from the ACE SWEPAM data set.

	v_r	$\log(S_p)$	B_{mag}/n_p	n_p	T_p	B_{mag}	$\log(\alpha/p)$	$\log(C^{6+}/C^{4+})$	$\log(C^{6+}/C^{5+})$	$\log(O^{7+}/O^{6+})$	$\log(Fe/O)$	$\log(f_{272})$
v_r	100	65	32	-12	63	36	4	-17	-26	-18	-16	24
$\log(S_p)$	65	100	58	-35	86	21	-20	-1	-5	-5	3	20
B_{mag}/n_p	32	58	100	-52	40	35	-34	28	21	25	4	34
n_p	-12	-35	-52	100	10	44	13	1	2	-4	-2	21
T_p	63	86	40	10	100	46	-18	4	0	-2	4	32
B_{mag}	36	21	35	44	46	100	-15	29	20	18	-2	68
$\log(\alpha/p)$	4	-20	-34	13	-18	-15	100	-20	-18	-11	-14	-16

log(C^{6+}/C^{4+})	-17	-1	28	1	4	29	-20	100	95	80	14	29
log(C^{6+}/C^{5+})	-26	-5	21	2	0	20	-18	95	100	76	13	22
log(O^{7+}/O^{6+})	-18	-5	25	-4	-2	18	-11	80	76	100	19	21
log(Fe/O)	-16	3	4	-2	4	-2	-14	14	13	19	100	-1
log(f_{272})	24	20	34	21	32	68	-16	29	22	21	-1	100

Table 7. The Pearson linear correlation coefficients between various quantities in the Ulysses polar passes of Table 3. The polar passes are cleaned to ensure only unperturbed coronal-hole plasma is included. Polar Crossing 3 (2000) and Polar Crossing 4 (2001) are eliminated and the comet McNaught interval (Days 35-41 of 2007) were eliminated from Polar Crossing 5. After cleaning, 79100 measurement time values remain for the correlations.

	v_r	log(S_p)	$v_A r$	$n_p r^2$	$n_a r^2$	$T_p r^{4/3}$	$B_{mag} r^2$	log(α/p)
v_r	100	31	2	5	14	40	8	15
log(S_p)	31	100	26	-48	-16	65	-16	33
$v_A r$	2	26	100	-13	-7	9	56	11
$n_p r^2$	5	-48	-13	100	66	24	44	-21
$n_a r^2$	14	-16	-7	66	100	28	19	22
$T_p r^{4/3}$	40	65	9	24	28	100	17	11
$B_{mag} r^2$	8	-16	56	44	19	17	100	-10
log(α/p)	15	33	11	-21	22	11	-10	100

Table 8. Estimates of the photospheric velocities of the solar-wind-origin footpoints for the Helios 1 and 2, ACE, Wind, and Ulysses spacecraft in the unperturbed coronal-hole plasma intervals of this study.

	r	θ_{lat}	v_{nadir}	v_{photo}	$\tau_{supergranule}$
Ulysses Polar Crossings	2 AU	80°	0.25 km/s	0.25 km/s	33 hr
ACE and Wind	1 AU	0°	1.9 km/s	0.5 km/s	17 hr
Helios at 0.6 AU	0.6 AU	0°	1.8 km/s	0.45 km/s	19 hr
Helios at 0.3 AU	0.3 AU	0°	1 km/s	0.25 km/s	33 hr

Author Manuscript
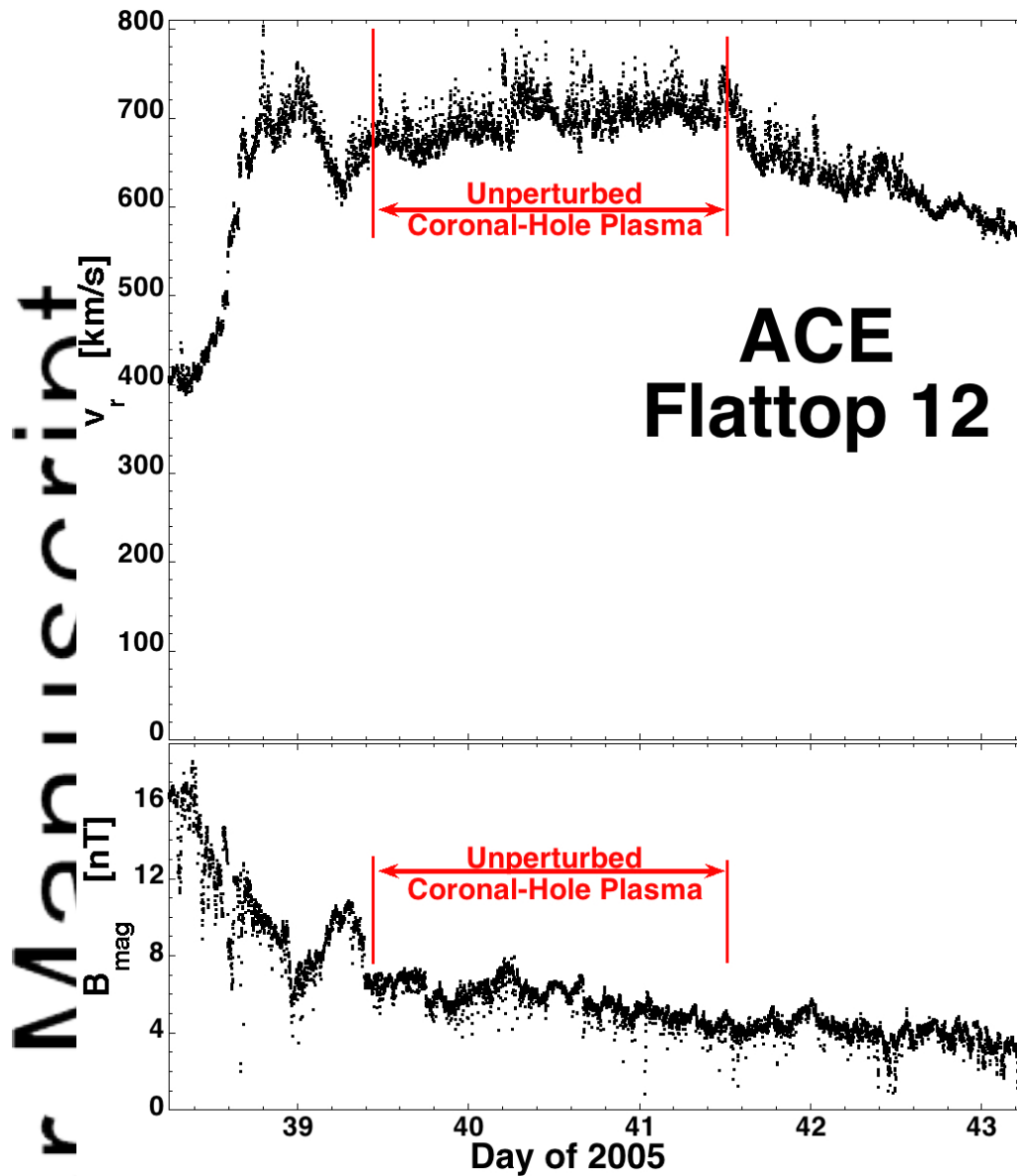
Figure 1. An example of a flattop high-speed stream at 1 AU as observed by ACE in 2005. In the top panel the radial velocity of the solar wind is plotted with 64-s time resolution and the interval of unperturbed coronal-hole plasma is indicated with the red double arrow and in the bottom panel the magnetic-field strength is plotted with 64-s time resolution.
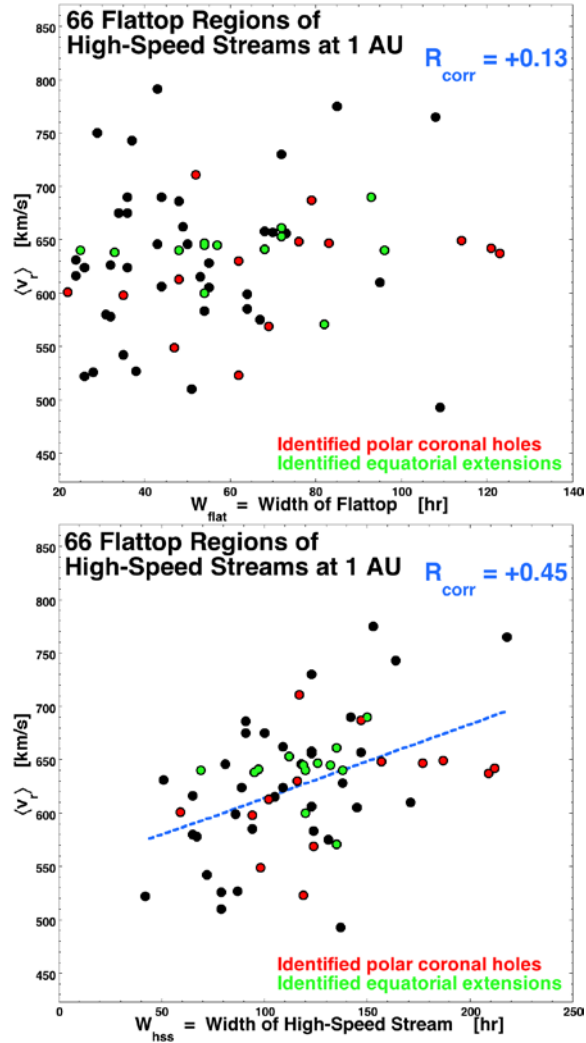
Figure 2. For the 66 intervals of unperturbed coronal-hole plasma at 1 AU, the average solar-wind radial velocity for each interval is plotted as a function of the width of the unperturbed interval (top panel) and as a function of the width of the high-speed stream (bottom panel). Red and green centers indicate the categorization of the high-speed streams by *Ko et al.* [2014]
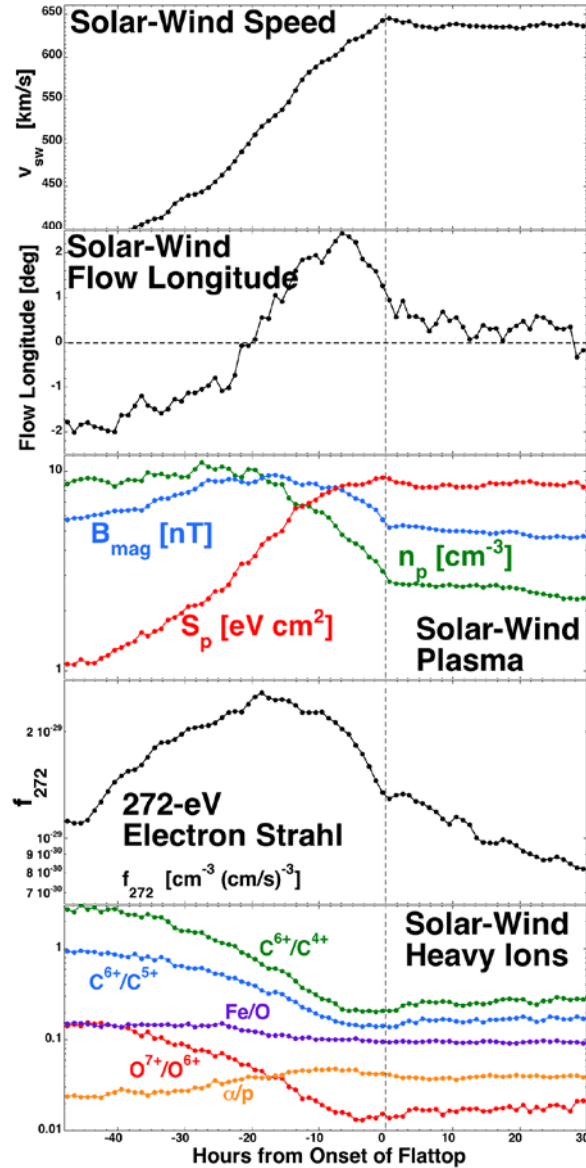
Figure 2. Superposed-epoch averages for solar-wind quantities for the 66 intervals of unperturbed coronal-hole plasma at AU. The zero epoch (trigger) is the onset time of each interval of unperturbed coronal-hole plasma. All quantities are from OMNI2 except f272 (from ACE SWEPAM) and the heavy-ion measurements (bottom panel) from ACE SWICS.
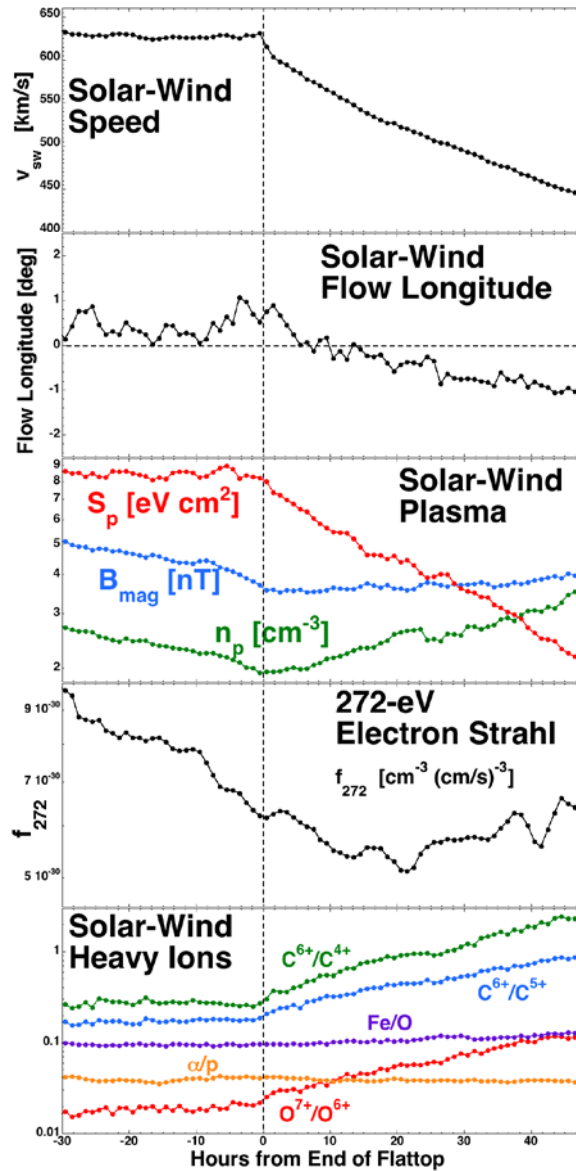
Figure 4. Superposed-epoch averages for solar-wind quantities for the 66 intervals of unperturbed coronal-hole plasma at AU. The zero epoch (trigger) is the termination time of each interval of unperturbed coronal-hole plasma. All quantities are from OMNI2 except f272 (from ACE SWEPAM) and the heavy-ion measurements (bottom panel) from ACE SWICS.
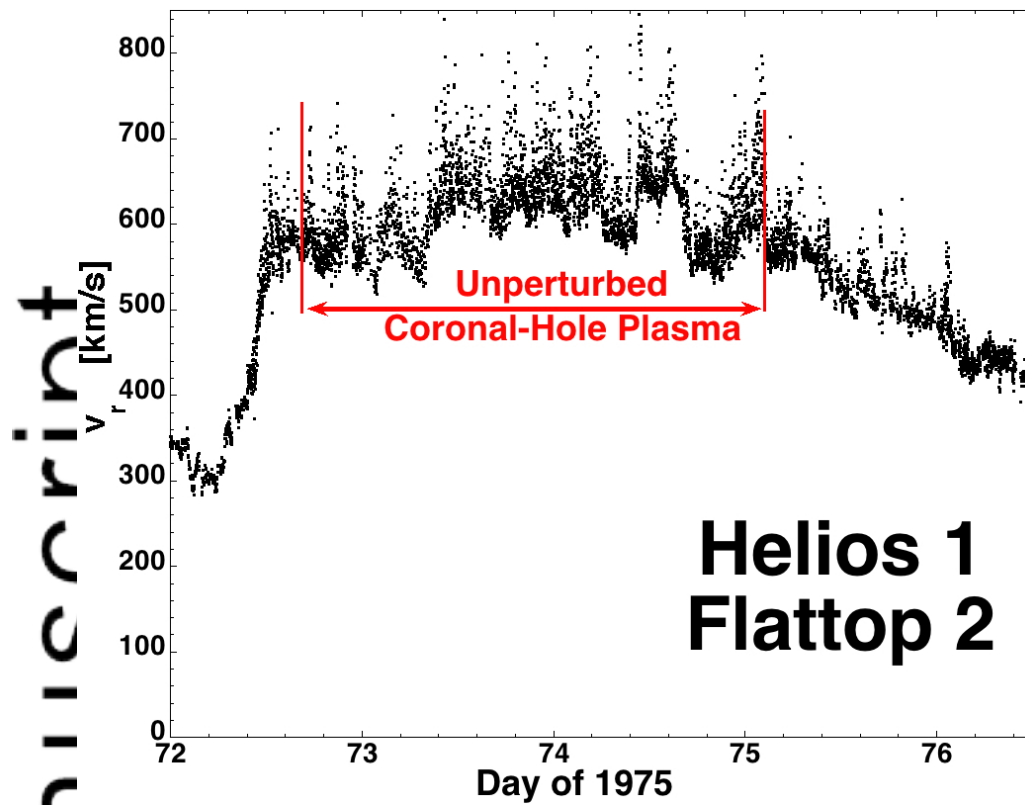
Figure 5. An example of a flattop high-speed stream at ~0.3 AU as observed by Helios 1 in 1975. The radial velocity of the solar wind is plotted with 40-s time resolution and the interval of unperturbed coronal-hole plasma is indicated with the red double arrow.
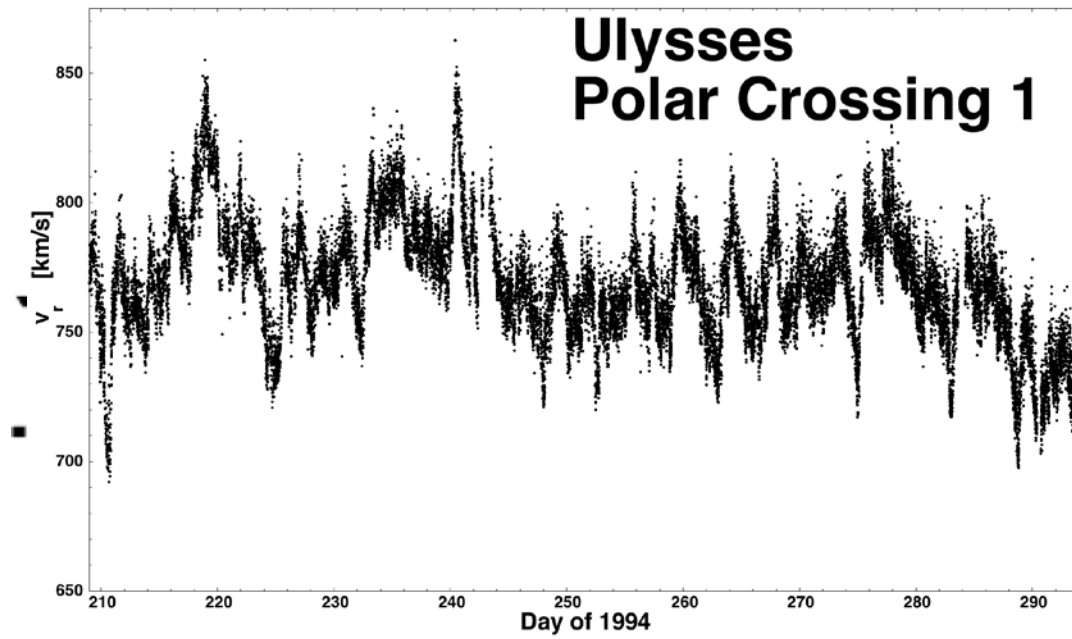
Figure 6. An example of an interval of unperturbed coronal-hole plasma at ~2 AU as observed by Ulysses in 1994. The radial velocity of the solar wind is plotted with 64-s time resolution. The entire plotted interval is unperturbed coronal-hole plasma.
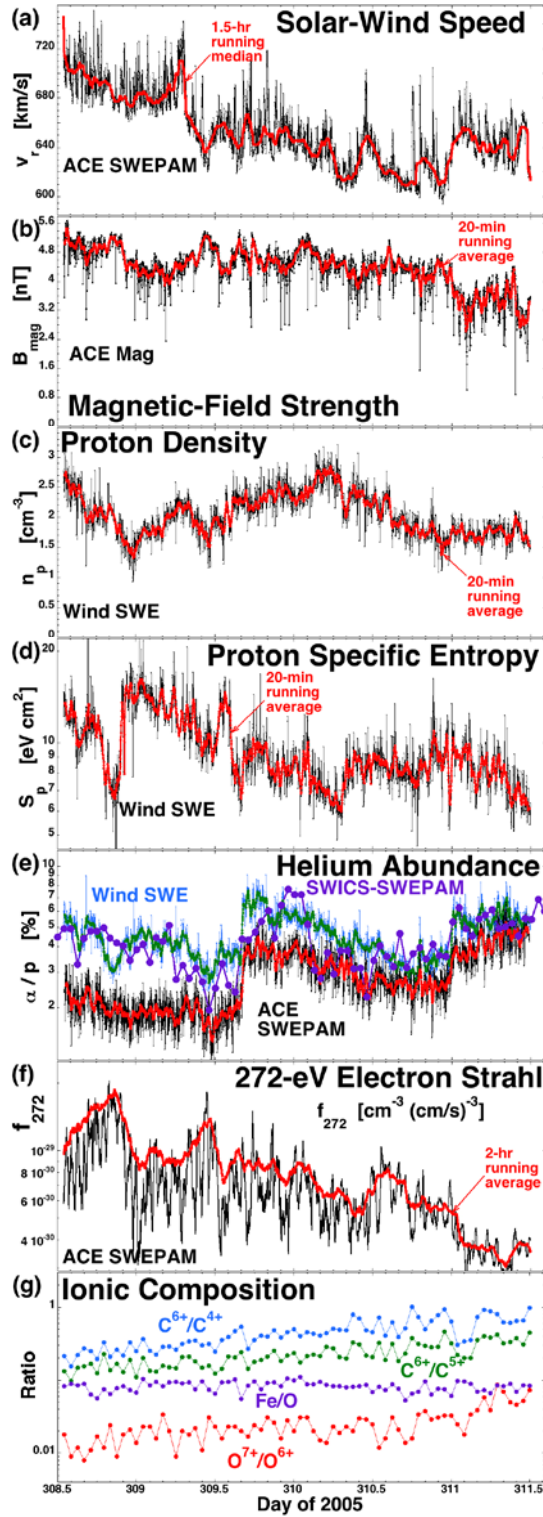
Figure 7. As examples of the structure in coronal-hole-origin solar wind, a number of measured quantities are plotted as a function of time during an interval (Flattop 15) of unperturbed coronal-hole plasma at 1 AU.
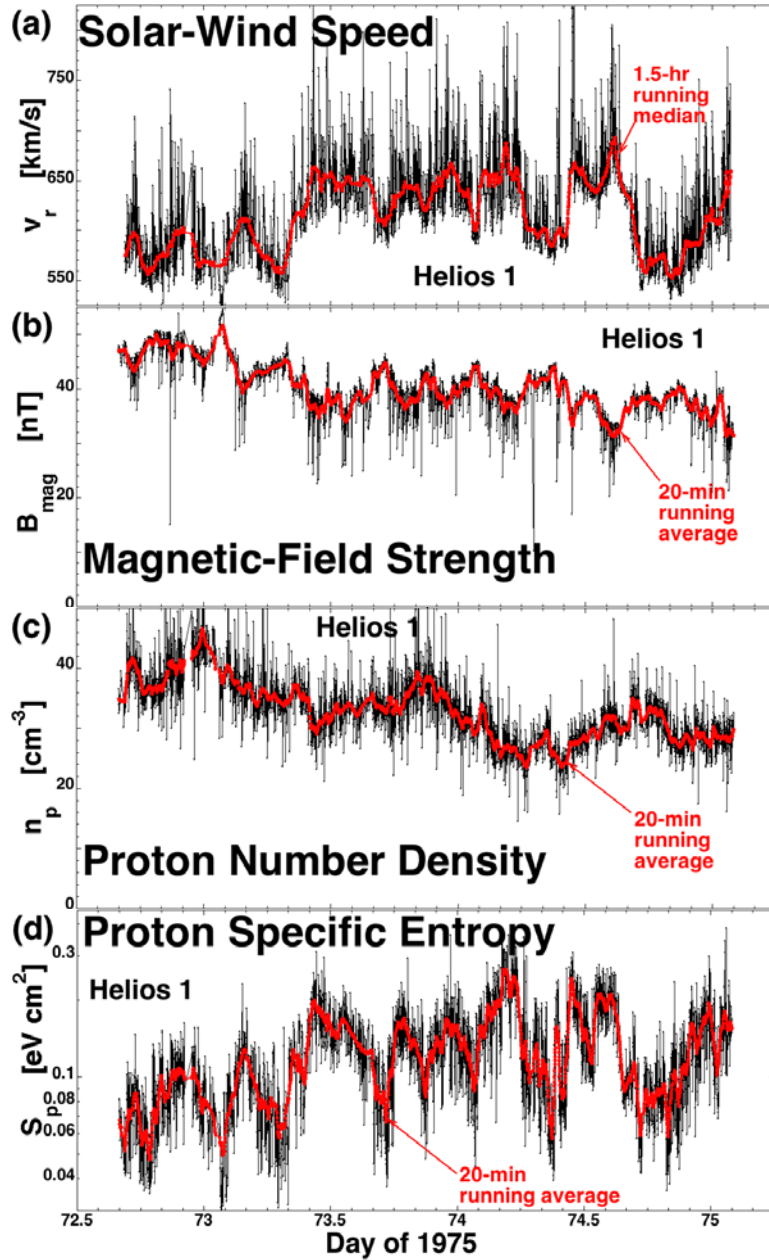
Figure 8. As examples of the structure in coronal-hole-origin solar wind, a number of measured quantities are plotted as a function of time during an interval (Helios Flattop Interval 2) of unperturbed coronal-hole plasma at 0.31 AU.

(a) Solar-Wind Speed

v_r [km/s]

810
770
730

Ulysses

1.5-hr running median

(b) Magnetic-Field Strength

B_{mag} [nT]

2
1.5
1
0.5
0

Ulysses

20-min running average

(c)

Ulysses

n_p [cm^{-3}]

0.6
0.4
0.2
0

20-min running average

Proton Number Density

(d) Proton Specific Entropy

S_p [eV cm^2]

30
20

Ulysses

20-min running average

(e)

Ulysses

α / p [%]

7
6
5
4
3
2
1
0

20-min running average

Helium Abundance

256   257   258   259   260
Day of 1994
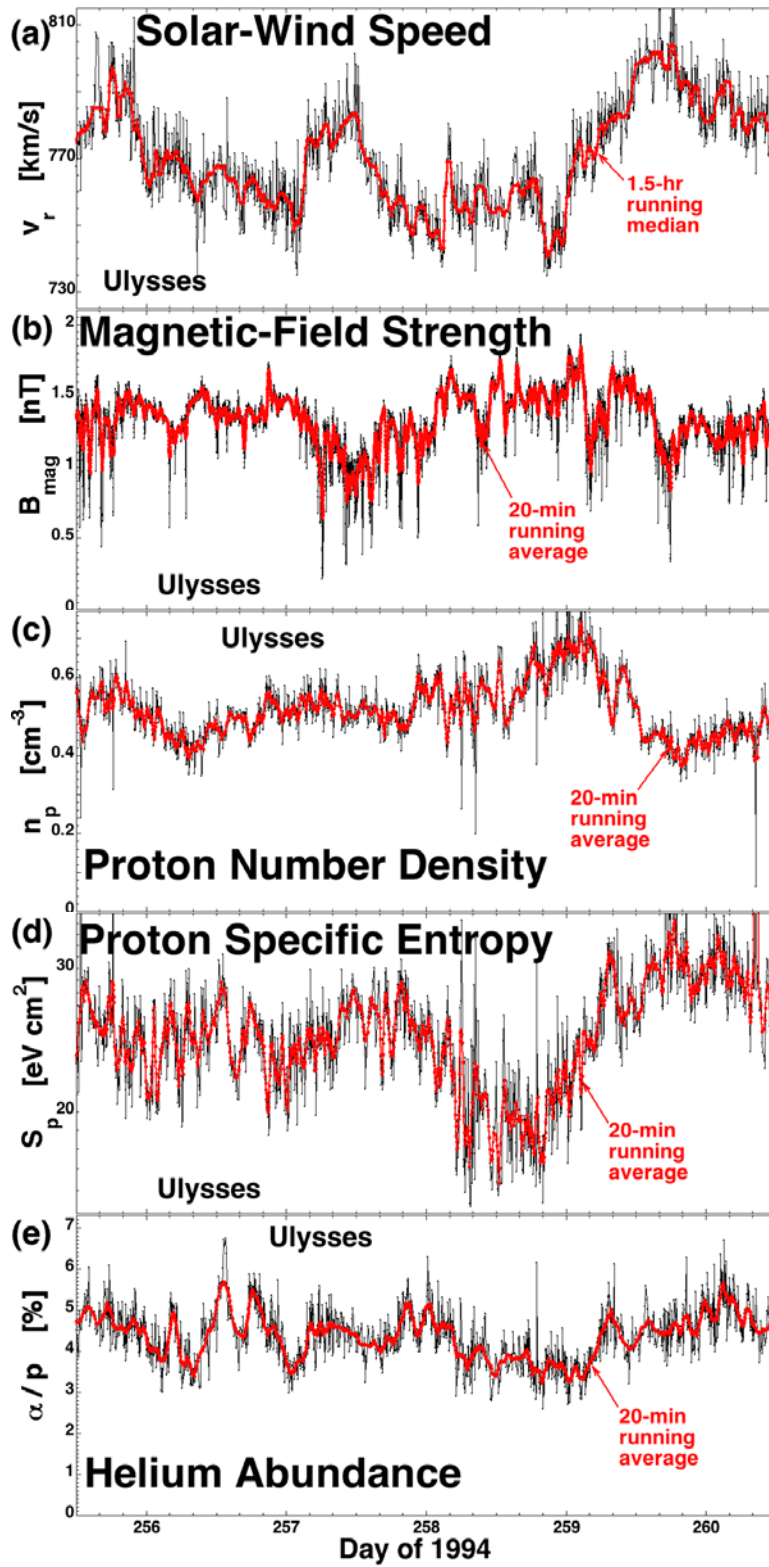
Figure 9. As examples of the structure in coronal-hole-origin solar wind, a number of measured quantities are plotted as a function of time during an interval (the five days of the highest-latitude portion of Polar Crossing1) of unperturbed coronal-hole plasma at 2.3 AU.

Author Manuscript
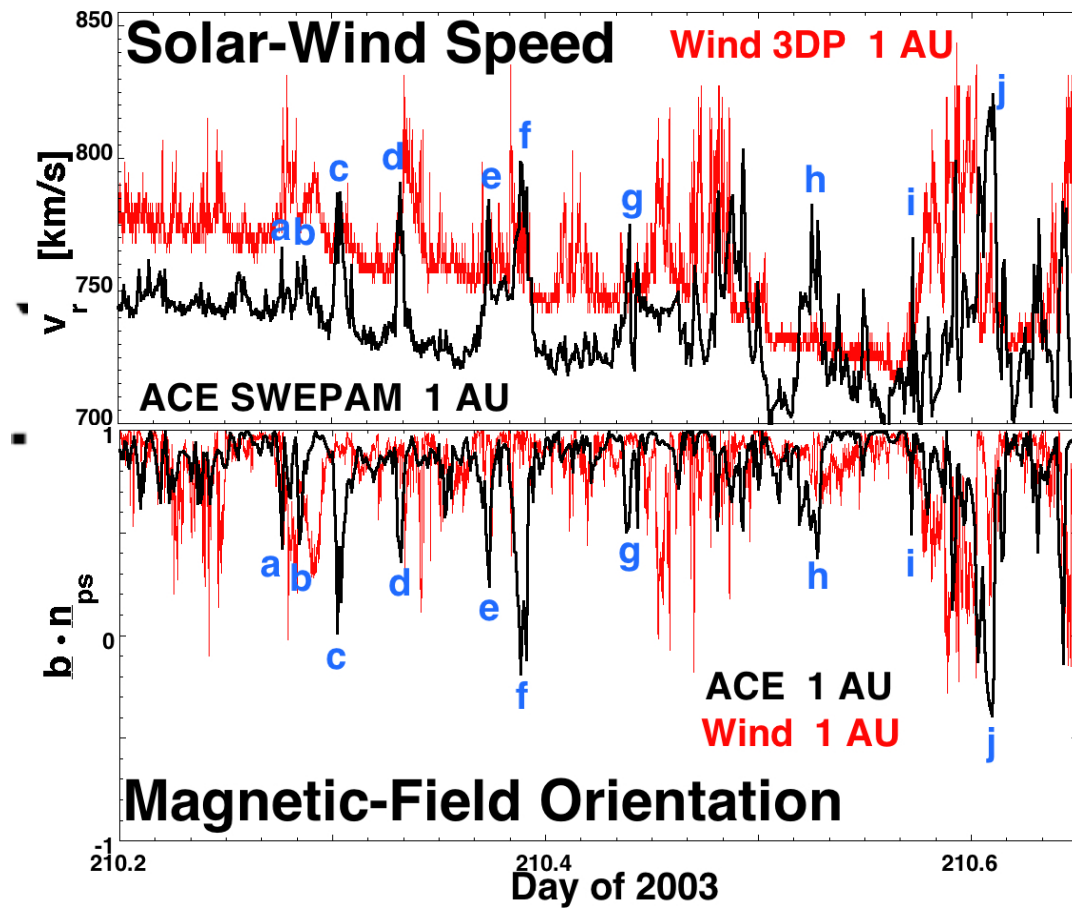
Figure 10. Magnetic-field foldings and the associated solar-wind-velocity pulses at 1 AU. The black curves are 64-s resolution measurements by ACE and the red curves are 3-s measurements by Wind during Flattop 5. ACE and Wind separated by ~ 70 R_E transverse to the Sun-Earth line and Wind is closer to the Earth.
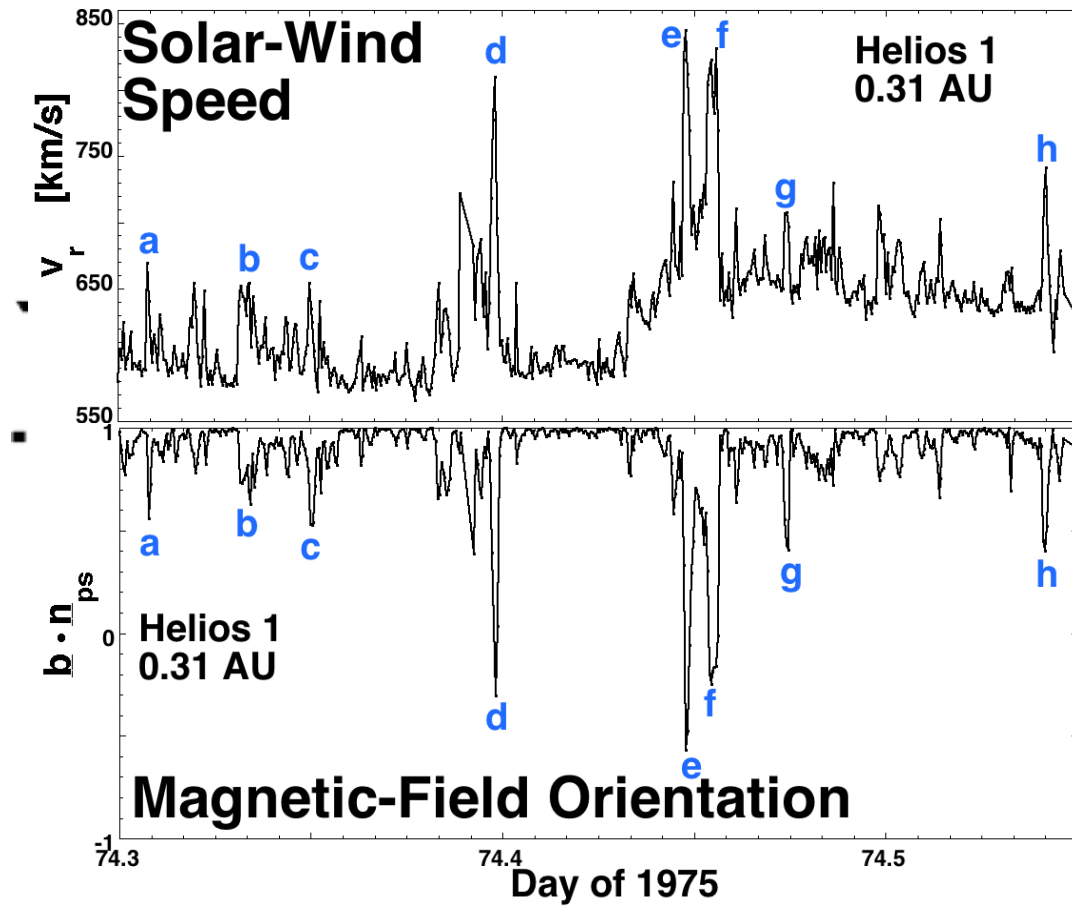
Figure 11. Magnetic-field foldings and the associated solar-wind-velocity pulses at 0.31 AU. The curves are 40-s resolution measurements by Helios 1 during Flattop Interval 2.
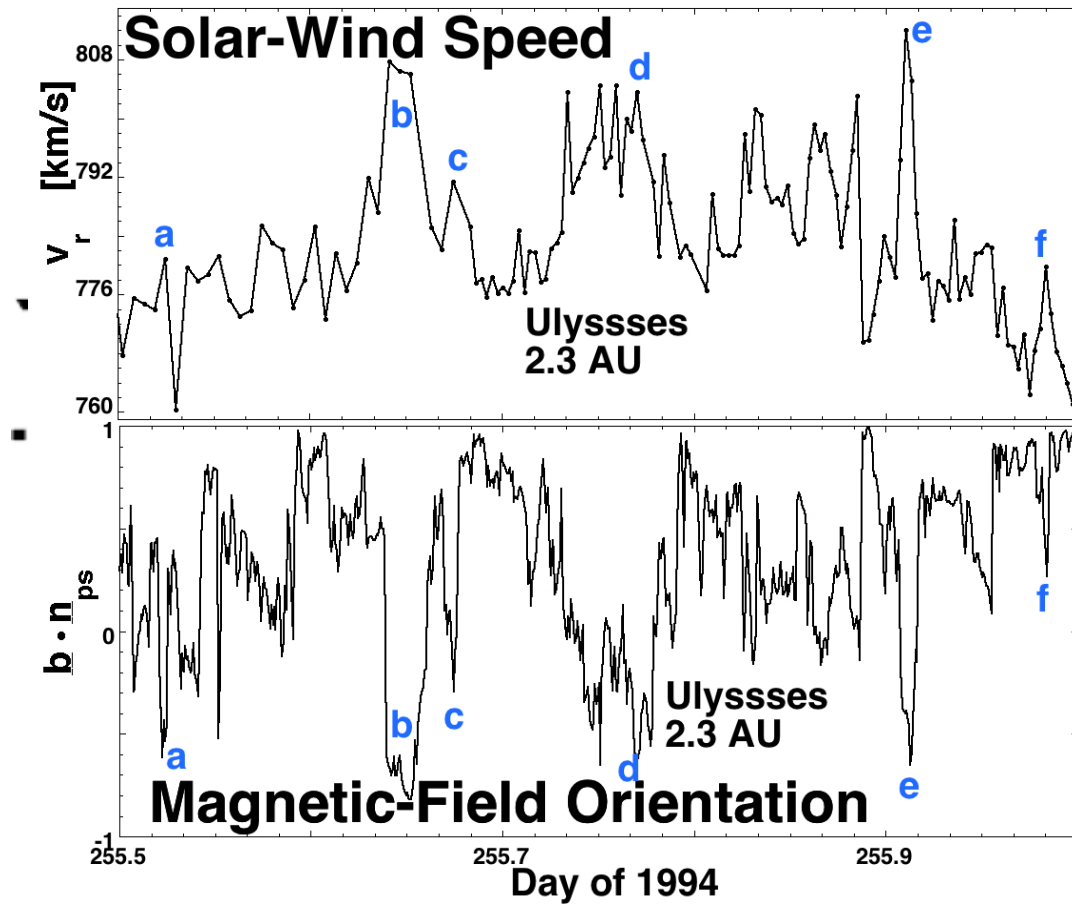
Figure 12. Magnetic-field foldings and the associated solar-wind-velocity pulses at 2.3 AU during Polar Crossing 1. The curve in the top panel is 4-min-resolution Ulysses plasma measurements and the curve in the bottom panel is 1-min-resoultion Ulysses magnetic-field measurements .
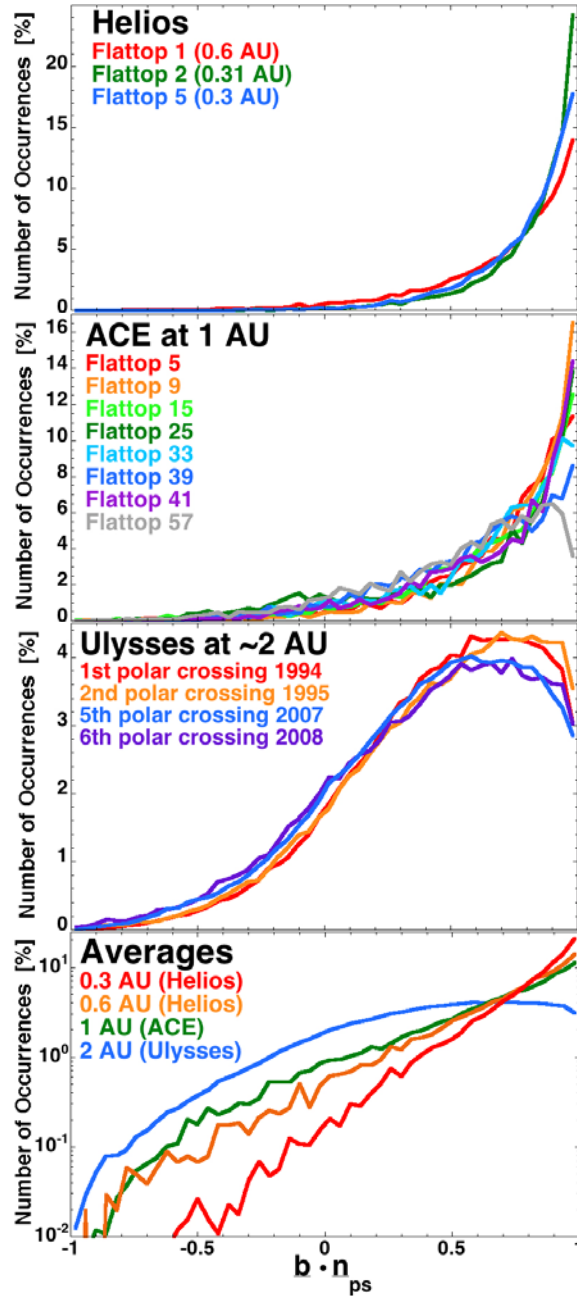
Figure 13. The deviation of the solar-wind magnetic field from the Parker-spiral direction $\underline{b}\bullet\underline{n}_{ps}$ is binned for the Helios 0.3 AU and 0.6 AU intervals of unperturbed coronal-hole plasma in the top panel, for a sampling of the ACE 1 AU intervals in the second panel, and for the Ulysses ~2 AU intervals in the third panel. In the bottom panel summations of the four collections of $\underline{b}\bullet\underline{n}_{ps}$ values are plotted logarithmically to see the progression of the distribution with distance from the Sun.
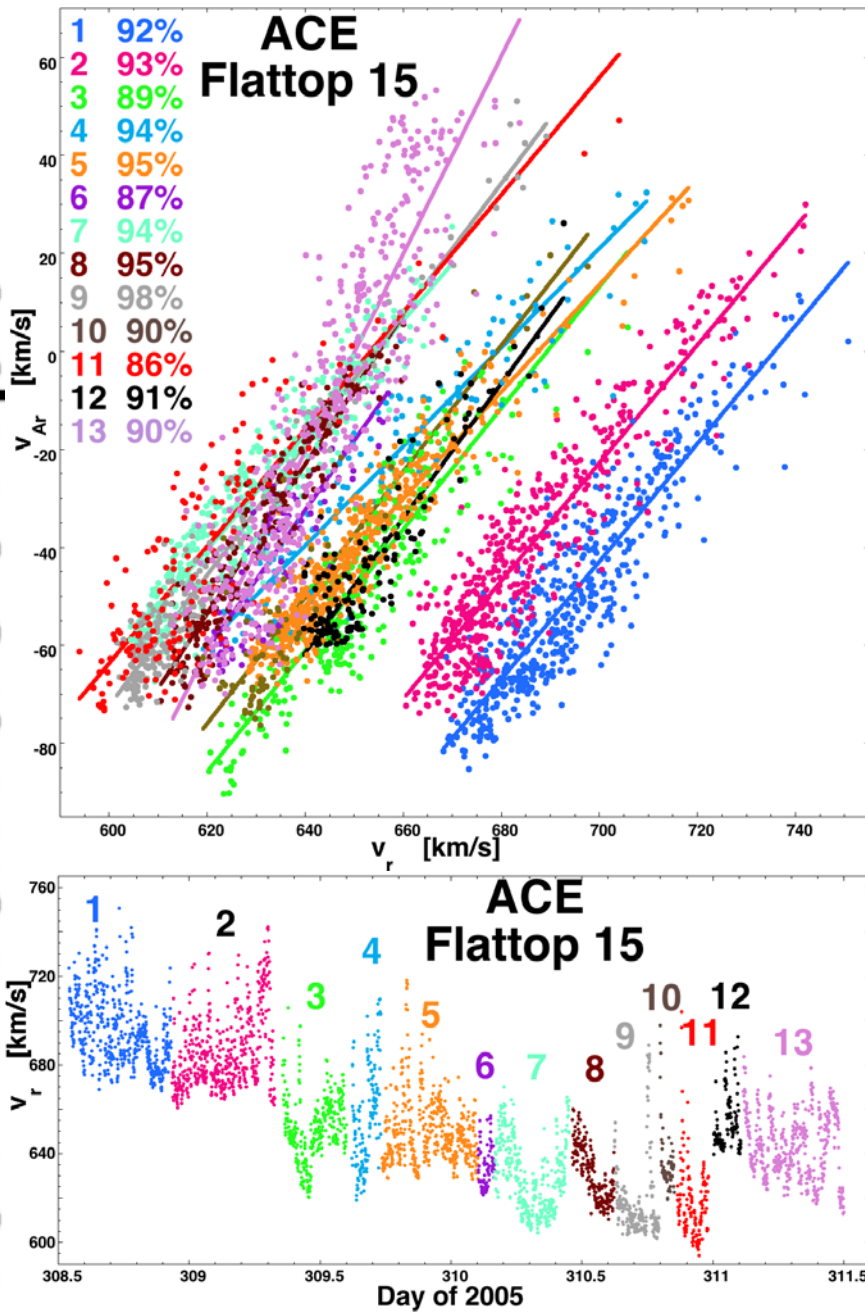
Figure 14. In the top panel, for the unperturbed coronal-hole plasma interval Flattop 15, the radial component of the solar-wind magnetic field v_{Ar} in Alfven units is plotted as a function of the radial flow velocity v_r; the data are broken into 13 domains of Alfvenicity denoted by the 13 colors. Linear regression fits for each domain are plotted as the colored lines and the linear correlation coefficient between v_{Ar} and v_r is listed for each domain. In the bottom panel v_r is plotted as a function of time for Flattop 15 with the points of each of the 13 Alfvenicity domains plotted in different colors.
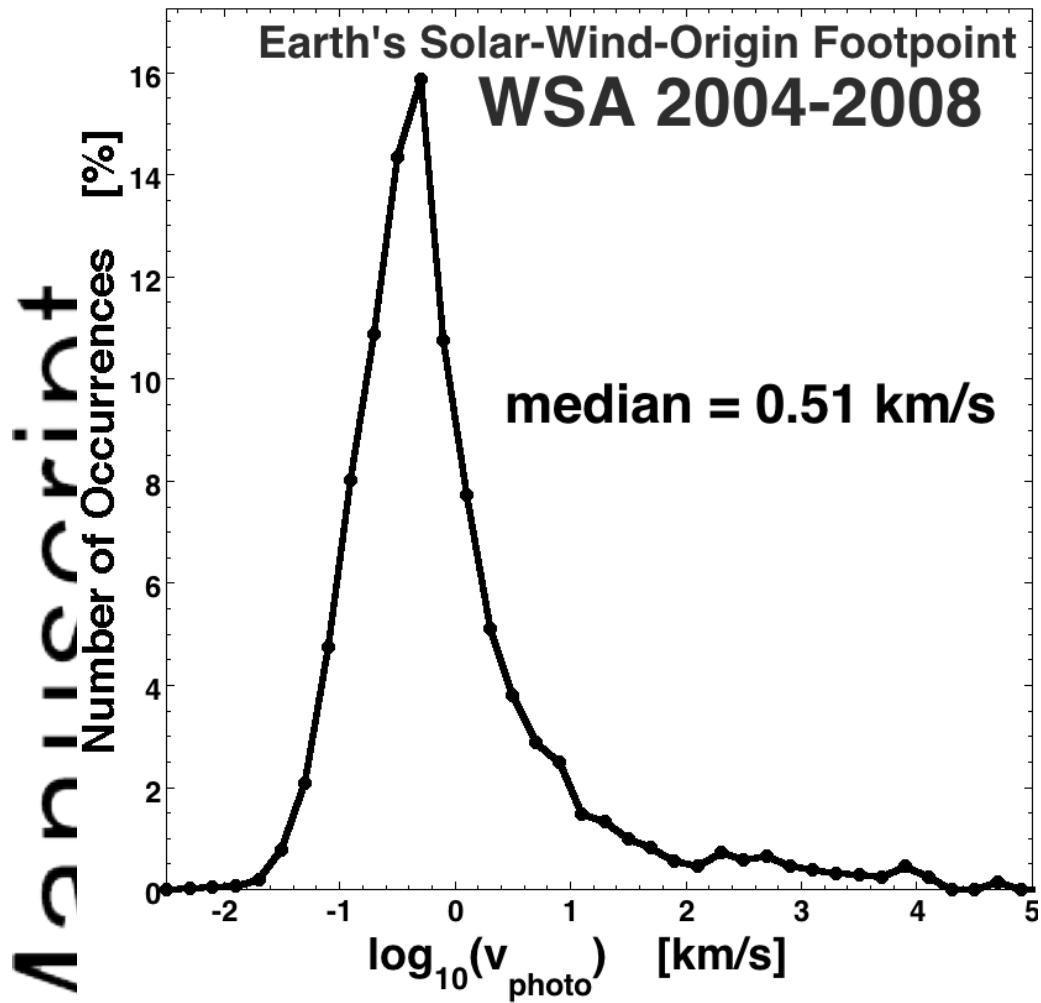
Figure 15. The velocity on the photosphere of the Wang-Sheeley-Arge-mapped solar-wind footpoint of the Earth is binned for the years 2004-2008. (Data courtesy of Nick Arge, 2009).
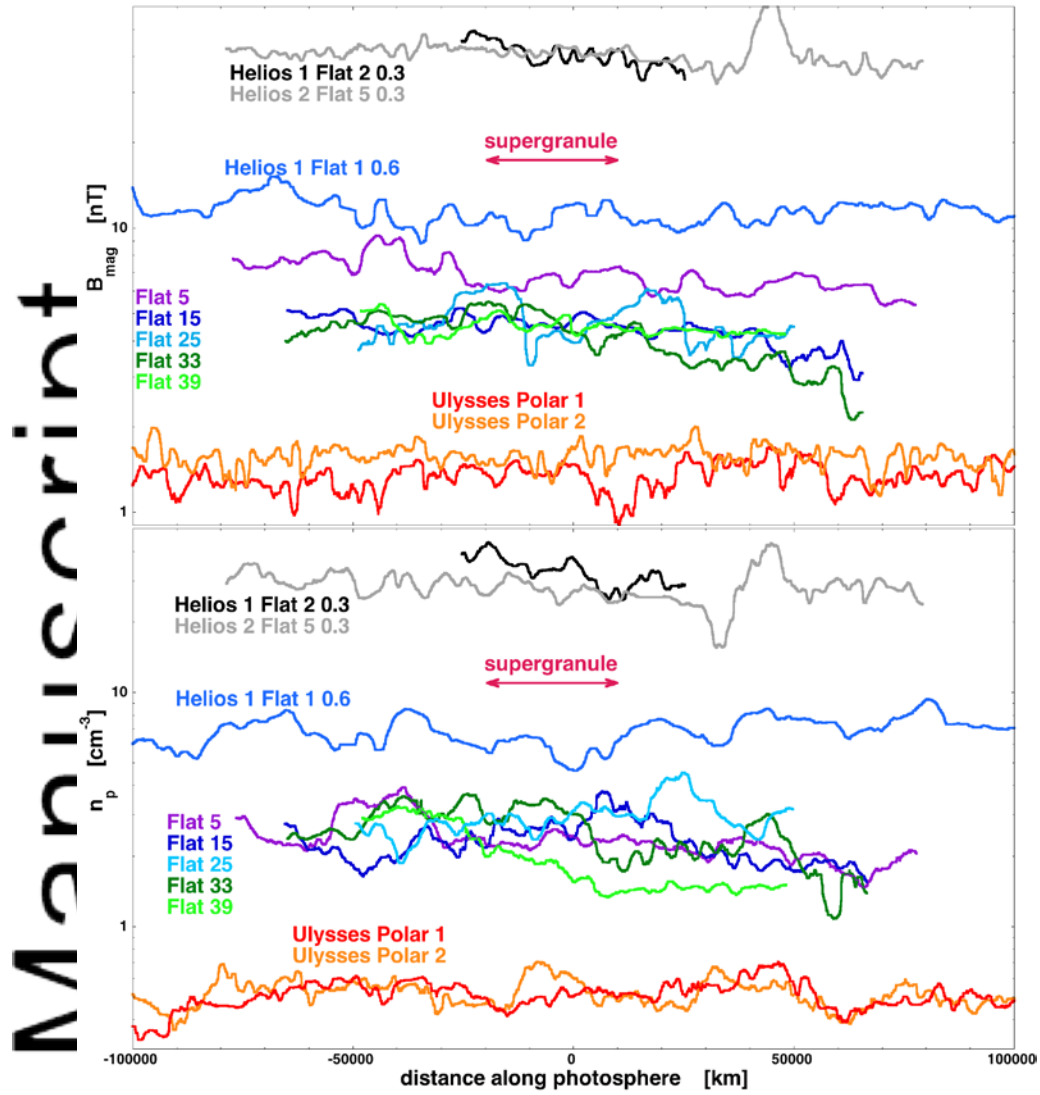
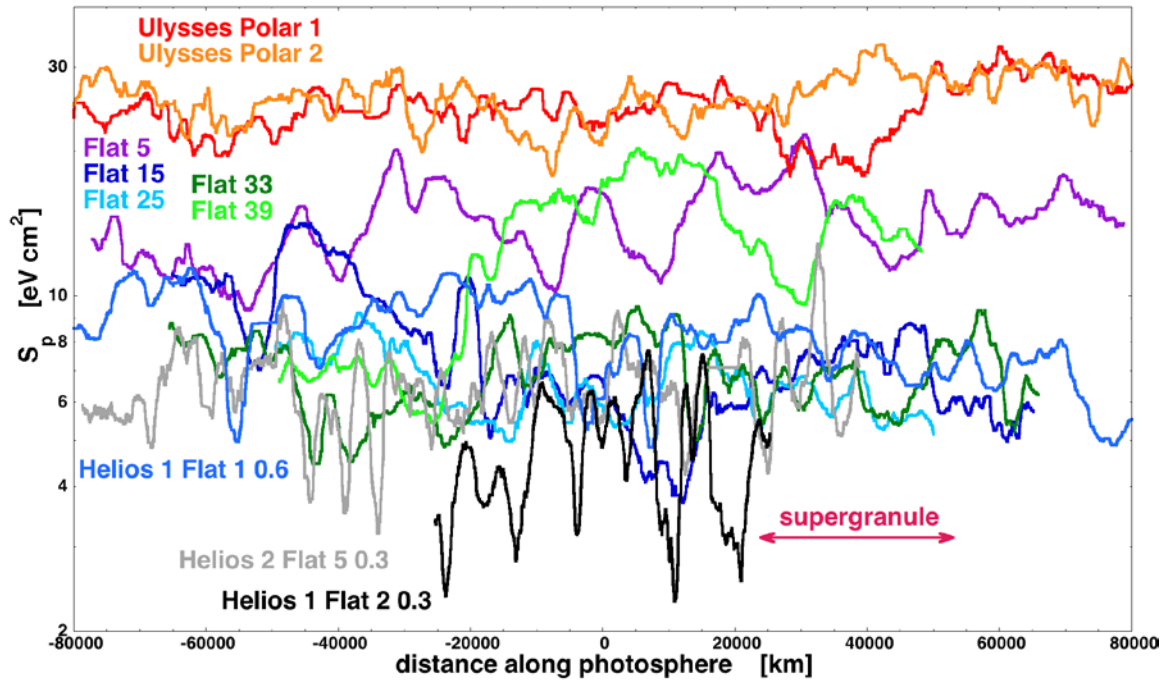Figure 16. Structure in the coronal-hole-origin solar wind as seen in the magnitude B_{mag} of the magnetic field from spacecraft measurements from 0.3 AU to ~2.3 AU in the top panel and structure in the coronal-hole-origin solar wind as seen in the proton number density n_p from spacecraft measurements from 0.3 AU to ~2.3 AU in the bottom panel. The measurement time series have all been converted to approximate distance along the photosphere of the solar-wind-origin footpoint for each spacecraft. The approximate size of a supergranule on the photosphere is indicated by the red double arrows.
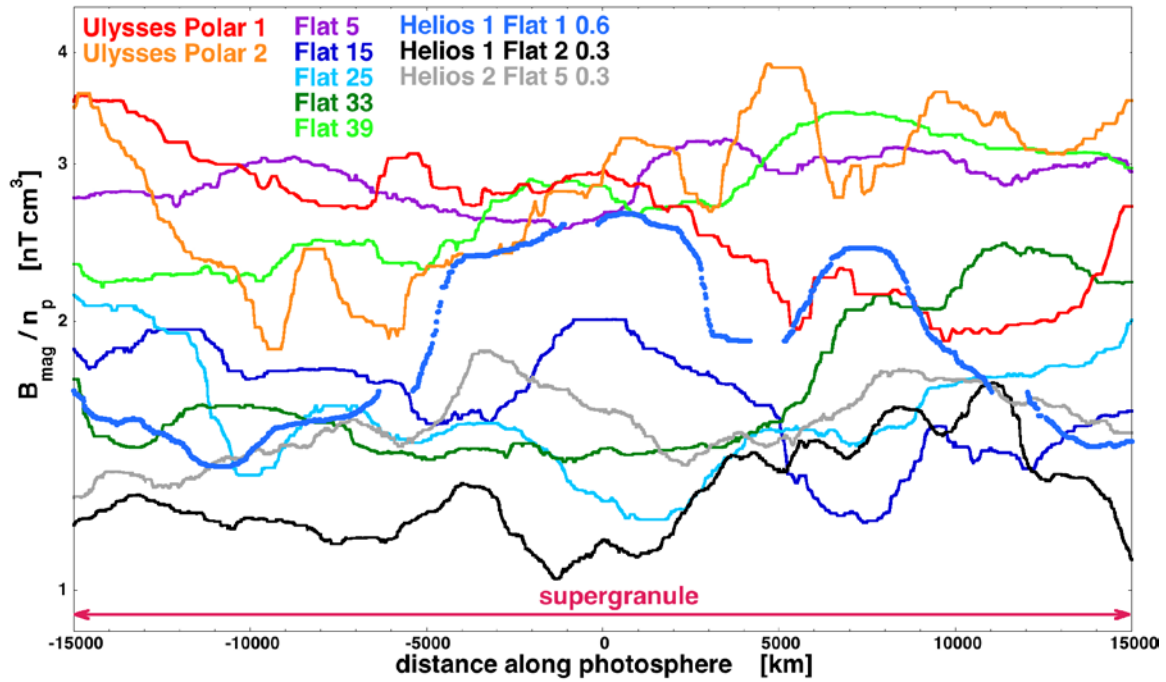
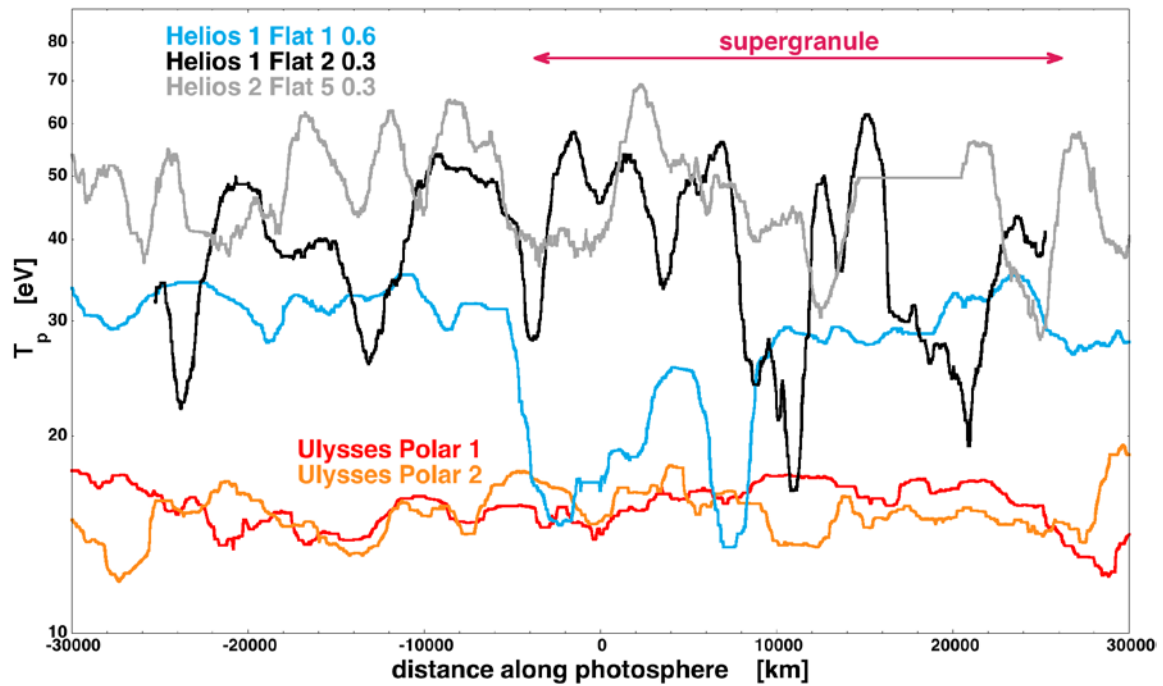Figure 17. Structure in the coronal-hole-origin solar wind as seen in the ratio B_{mag}/n_p from spacecraft measurements from 0.3 AU to ~2.3 AU. The measurement time series have all been converted to approximate distance along the photosphere of the solar-wind-origin footpoint for each spacecraft. The approximate size of a supergranule on the photosphere is indicated by the red double arrows.

Figure 18. Structure in the coronal-hole-origin solar wind as seen in the proton specific entropy S_p from spacecraft measurements from 0.3 AU to ~2.3 AU. The evolution with distance of the entropy is also seen. The measurement time series have all been converted to approximate distance along the photosphere of the solar-wind-origin footpoint for each spacecraft. The approximate size of a supergranule on the photosphere is indicated by the red double arrows.
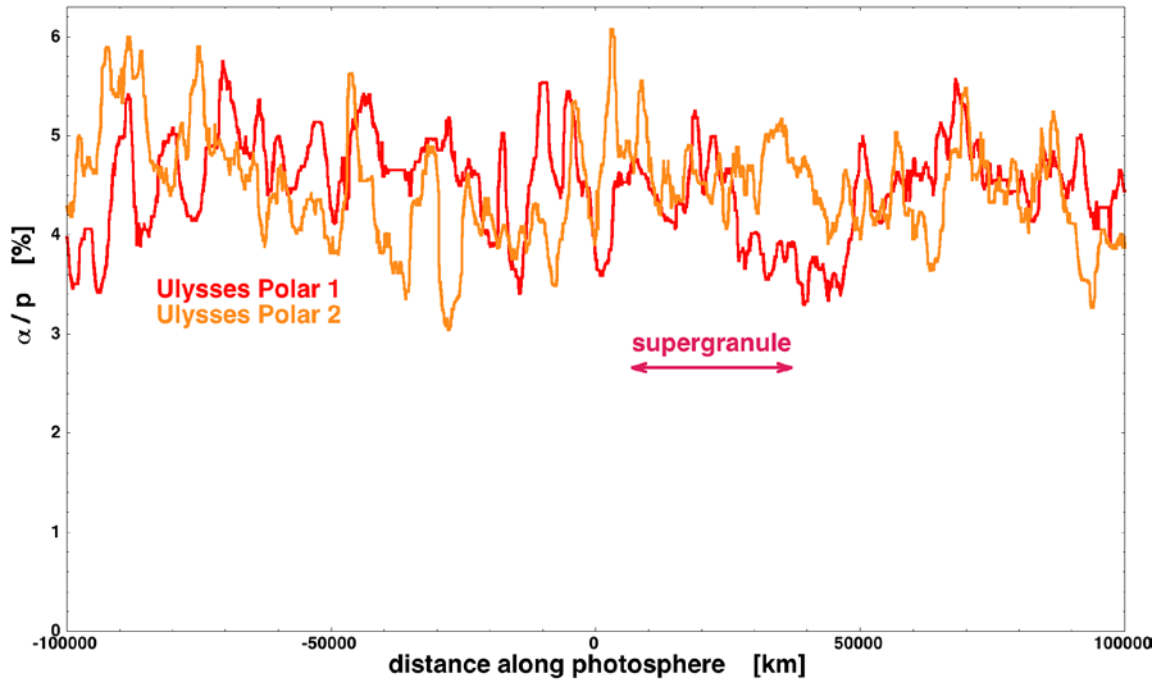
Figure 19. Structure in the coronal-hole-origin solar wind as seen in the proton temperature T_p from spacecraft measurements from 0.3 AU to ~2.3 AU. The evolution with distance of the temperature is also seen. The measurement time series have all been converted to approximate distance along the photosphere of the solar-wind-origin footpoint for each spacecraft. The approximate size of a supergranule on the photosphere is indicated by the red double arrows.

Figure 20. Structure in the coronal-hole-origin solar wind as seen in the helium abundance α/p S_p from Ulysses measurements at ~2.3 AU. The measurement time series have been converted to approximate distance along the photosphere of the solar-wind-origin footpoint for Ulysses. The approximate size of a supergranule on the photosphere is indicated by the red double arrows.
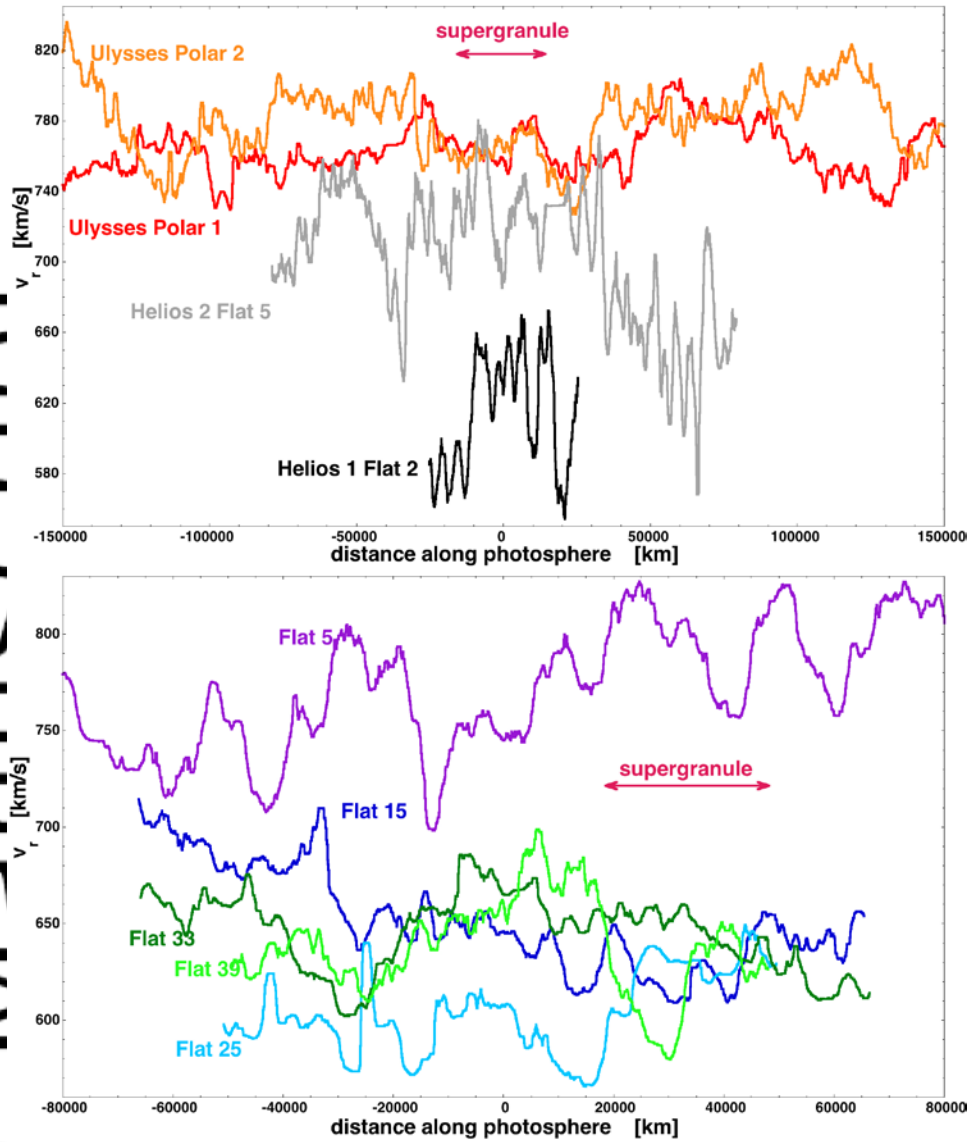
Figure 21. In the top panel structure in the coronal-hole-origin solar wind as seen in the solar-wind velocity v_r from Helios measurements at ~0.3 AU and Ulysses measurements at ~2.3 AU and in the bottom panel structure in the coronal-hole-origin solar wind as seen in the solar-wind velocity v_r from ACE measurements at 1 AU. The measurement time series have all been converted to approximate distance along the photosphere of the solar-wind-origin footpoint for each spacecraft. The approximate size of a supergranule on the photosphere is indicated by the red double arrows.
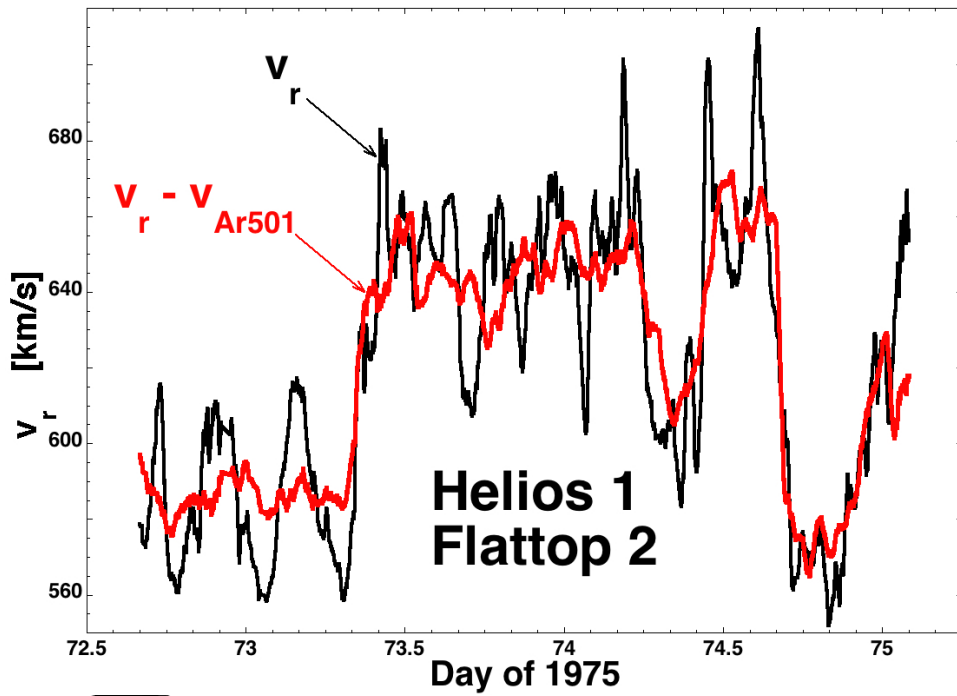
Figure 22. In black the measured solar-wind velocity vr is plotted and in red the solar-wind velocity with Alfvenic fluctuation subtraction is plotted. For the subtracting, a 3.3-hr baseline is used, so only Alfvenic fluctuations shorter than 3.3 hr are removed. Both curves are 33-minute running averages.
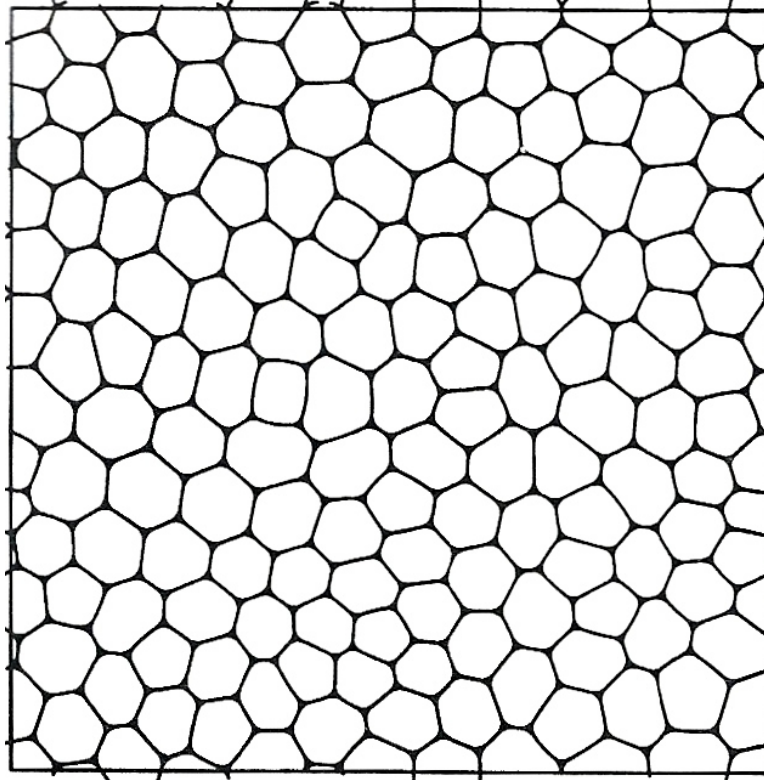
Figure 23. Looking in the radial direction outward from the Sun, a two-dimensional simulation of cellular structure (after Fig. 6.2a of *Weaire and Hutzler* [1999]) is used to represent a square area in the heliosphere filled with 150 funnels from the Sun. The box is 2.1 supergranules by 2.1 supergranules in size, which is 5.2^{o} by 5.2^{o}.